Title

Scalable mapping and monitoring of Mediterranean-climate oak landscapes with temporal mixture models

Authors

Sousa, Daniel
Davis, Frank W

Publication Date

2020-09-01

DOI

10.1016/j.rse.2020.111937

Peer reviewed

Scalable mapping and monitoring of Mediterranean-climate oak landscapes with temporal mixture models

Daniel Sousa[1*] and Frank Davis[1]

[1]*La Kretz Research Center at Sedgwick Reserve and National Center for Ecological Analysis and Synthesis, Earth Research Institute, UC Santa Barbara, Santa Barbara, CA 93101, USA.* [*]*sousa@nceas.ucsb.edu*

Abstract

Mediterranean-climate oak woodlands are prized for their biodiversity, aesthetics, and ecosystem services. Conservation and maintenance of these landscapes requires accurate observations of both present and historic conditions capable of spanning millions of hectares. Decameter optical satellite image time series have the observational coverage to meet this need, with almost 40 years of intercalibrated global observations from the Landsat program alone. Despite this wealth of data, the optimal approach to leverage these observations for oak ecosystem monitoring remains elusive. Temporal mixture models (TMMs) may offer a solution. TMMs use a linear inverse model based on temporal endmembers (tEMs) chosen to optimize both parsimony and information content by 1) possessing clear biophysical meaning, and 2) accurately representing the variance structure of the observations as determined by Euclidean position in the temporal feature space (TFS) composed of low-order Principal Components. We apply this approach to the California Sierra foothill oak system. Low-order TFS structure across the entire Sierra Foothill study area is consistently bounded by 4 tEM phenologies: annual grasses, evergreen perennials, deciduous perennials + shadow, and unvegetated areas. Satellite-based tEM phenologies correspond to ground-based PhenoCam time series (correlations 0.8 to 0.9). Systematic temporal decimation is conducted to simulate years with varying numbers of cloud free measurements. Fractions are observed to scale linearly using as few as 6 images per year and coarse feature space topology is retained with as few as 4 (well-timed) images per year. The effect of 10 m versus 30 m pixel resolution is investigated. Linear scaling is observed with correlations in the 0.78 to 0.95 range. Comparison of 10 m Sentinel-2 fractions to LiDAR-derived tree abundance at San Joaquin Experimental Range shows a correlation of 0.74. Visual orthophoto validation shows accuracies of annual, deciduous, and evergreen fractions in the 74 to 88% range (n = 102). Multi-year analysis of August imagery at Sequoia National Park to investigate dynamics associated with the 2011-2017 drought reveals 5 tEMs corresponding to: steady growth, steady decline, early decline then regrowth, persistent vegetation, and no vegetation. Validation images are sparse, but where available show accuracies in the 88 to 91% range for decrease, growth, and persistently vegetated fractions (n = 102). Decreases are observed in areas noted by a recent field-based study. The results of this analysis suggest the TMM approach has promise a novel, accurate, explainable, and linearly scalable method for retrospective analysis and prospective monitoring of Mediterranean-climate oak landscapes.

Keywords

Mediterranean ecosystems; California; Oak woodland; savanna; Phenology; Landsat; Sentinel

Introduction

Mediterranean-climate oak woodlands and savannas are the focus of considerable scientific, social, and aesthetic interest. Covering approximately 4 million hectares in California and 3 million hectares in Spain and Portugal (Marañón et al., 2009), oak systems host thousands of understory plant and animal species (California Department of Fish and Wildlife (CDFW), 2014; Guisti et al., 1996; Swiecki et al., 1997). As a consequence of their broad spatial extent and exceptional biodiversity, oak woodlands and savannas are a key component of the designation of both the California Floristic Province and Mediterranean Basin as global biodiversity hotspots (Baldwin, 2014; Myers et al., 2000). In addition to their ecological importance, Mediterranean-climate oak landscapes are also recognized for their intrinsic aesthetic and historic value (Allen-Diaz et al., 2007; Davis et al., 2016; Pavlik et al., 1993).

Maintaining Mediterranean-climate oak landscapes is challenging given the number of potential drivers of change. Some agents, such as drought and fire, have existed for millennia and may be amplifying (Davis and Borchert, 2006; Klausmeyer and Shaw, 2009; Loarie et al., 2008; Mensing, 2006; Miller et al., 2009). Other processes, like suburban sprawl (Cameron et al., 2014; Gaman and Firman, 2006) and introduction of nonnative pests (Swiecki et al., 1997), are more recent threats. The confluence of such factors, including observed low recruitment rates of some oak species (Tyler et al., 2006), could significantly alter the extent and composition of oak landscapes. Understanding both past and ongoing effects of these change drivers can both provide valuable context for predicting future impacts and help guide conservation efforts.

Quantitative evaluation of change at a landscape scale requires accurate and spatially extensive methods for both retrospective analysis and prospective monitoring. While optical remote sensing has been used for decades for this purpose, recent advances in data availability and quality have substantially increased the capability of satellite imaging systems. Many of these developments are associated with the Landsat program, including the opening of the Landsat archive (Wulder et al., 2012); rigorous radiometric intercalibration (Chander et al., 2009); subpixel geolocation and terrain correction (Storey et al., 2014); and standardized atmospheric correction routines (Vermote et al., 2018; Vermote and Saleous, 2007). In addition, the 2015 and 2016 launches of Sentinel-2a and -2b (Drusch et al., 2012), along with the European Space Agency's free data availability policy (Berger et al., 2012), provide increased spatial resolution and substantially shortened revisit time. Considerable effort has also been devoted to merging the Landsat and Sentinel-2 data streams, including the development of the Harmonized Landsat Sentinel-2 (HLS) product (Claverie et al., 2018). Taken together, these developments have been heralded as a "paradigm shift" in optical remote sensing (Woodcock et al., 2019), offering new opportunities to improve our understanding of oak landscapes in both California and the Mediterranean region.

Advances in imaging systems and data availability have been accompanied by a concomitant increase in research on remote sensing of oak woodlands and Mediterranean-climate ecosystems (Figure 1). A plethora of monitoring and analysis methods have been proposed for Mediterranean landscapes. Many of these methods are based on change detection

from image pairs or relatively small numbers of images (e.g. (Berberoglu and Akin, 2009; Recanatesi et al., 2018)). While useful for mapping changes associated with specific events, these methods do not fully exploit the dense image time series that are now available. Other methods focus on aerial orthophoto, imaging spectroscopy, and/or LiDAR surveys (e.g. (Asner et al., 2016; Bogan et al., 2019; Fricker et al., 2019; Miraglio et al., 2020; Navarro et al., 2019; Swatantran et al., 2011)). These studies have achieved impressive results, but remain spatially and temporally limited until data coverage expands considerably – and even then will not allow for retrospective analysis. Finally, highly generalized approaches to automated operational monitoring (e.g. (Koltunov et al., 2019; Verbesselt et al., 2010)) are under continuous development and can be a useful tool for land managers. However, they are intentionally designed not to be tailored to specific ecosystem types and can rely on algorithms with considerable complexity. The need still exists for a method that is tailored to oak woodland and savanna landscapes and can efficiently map and monitor change at regional scales using existing multispectral satellite image time series.

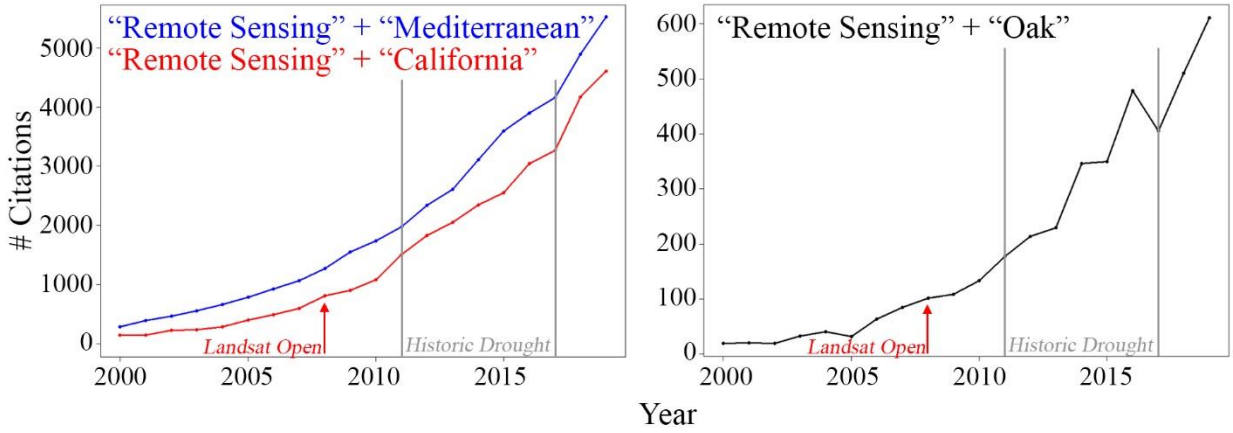

Figure 1. Citation history. Scientific interest in the remote sensing of Mediterranean landscapes (blue), remote sensing of California (red) and remote sensing of oaks (black), has shown a marked increase in recent years, as measured by number of citations in the Web of Science database associated with these keywords. Growth accelerated considerably following the 2008 opening of the Landsat archive (red arrows) and the 2011-2017 California drought (gray bars).

Temporal mixture models (TMMs) may offer a parsimonious solution. TMMs (Piwowar et al., 1998; Quarmby, 1992; Quarmby et al., 1992) represent each pixel time series as a linear combination of constituent endmember temporal processes. Using spatiotemporal characterization (Small, 2012) and knowledge of the landscape, the endmember processes can be chosen to represent straightforward, intuitive landscape components (e.g. distinct vegetation phenologies). Unlike many commonly used complex, multilayered statistical mapping algorithms, the TMM approach rates highly on the metric of "explainability" (Gunning, 2017), a factor deemed increasingly important by data scientists. TMMs are most useful when objects on the landscape are: 1) spatially mixed at the scale of the pixel, and 2) more distinct temporally than spectrally. These conditions are met in many Mediterranean-climate oak landscapes where plant communities may be spatially heterogeneous and spectrally indistinct, but phenologically variable. Previous studies have implemented TMMs for the mapping of impervious surfaces (Li

and Wu, 2014; Yang et al., 2012), arctic sea ice (Chi et al., 2016; Piwowar et al., 1998), seasonal cloud forest/grassland systems (Sousa et al., 2019), agricultural dynamics (Jain et al., 2013; Lobell and Asner, 2004; Quarmby et al., 1992; Sousa and Small, 2019), and tropical mangrove forests (Small and Sousa, 2019), with promising results. To our knowledge, however, TMMs remain untested both for Mediterranean systems in general and for California oak landscapes in particular.

In this work, we introduce the TMM approach to the mapping and monitoring of Mediterranean-climate oak landscapes. We focus on the California Sierra foothill oak system for reasons outlined below. Specifically, this work addresses the following questions:

1) *Characterization*: What are the dominant spatiotemporal modes of variability in these landscapes, as captured by decameter multispectral satellite image time series? Which, and how many, unique phenological signatures can be reliably identified? How do temporal endmembers derived from satellite image series compare to independent ground-based phenology measurements?
2) *Stability & Scaling*: How does this characterization change across the ~500 km extent of the study area? With decreased temporal sampling frequency? How do mapping results compare between 10 m (current & future Sentinel-2) and 30 m (historic & current Landsat) spatial scales?
3) *Validation and Comparison*: How does single-year mapping accuracy compare against canopy height models derived from small-footprint airborne LiDAR? How do estimates of drought-associated defoliation compare to airphotos and meter resolution satellite images?

Background

A. Study Area

The same landscape complexity that imparts much of the value of oak landscapes also substantially complicates monitoring efforts. Oak landscapes span a wide range of climate zones, elevations, soil types, and land ownership regimes. Individual oaks span a broad continuum of morphologies and sizes: for instance, oak canopies can range from shrublike, < 1 m diameter to arborescent, > 30 m diameter. Tree heights can also vary at a similar scale. Structurally, oak landscapes range from open, grass-dominated savannas with sparse tree cover to dense, closed canopy woodlands and forests. Trees can occur in monospecific or mixed stands. Oak species can be evergreen, seasonally deciduous, and/or drought-deciduous. Substantial phenologic variation exists within species and even within canopies of individuals. Any comprehensive analysis and monitoring approach must contend with this formidable multiscale complexity.

One approach to accommodate this diversity is to decompose the full spatial domain of oak woodlands and savannas into smaller subregions with more manageable properties. California's Sierra Nevada foothills (red outline in Figure 2) are one such subregion. On its own, the Sierra foothill system is both interesting and important for several reasons. A recent analysis has identified the Sierra foothills as facing particularly extensive threats from development (Gaman and Firman, 2006). Recent severe drought has also raised concerns of elevated rates of

oak mortality in the Sierra foothills due to its hot, dry summers and declining water table. In addition to its environmental and social importance, the Sierra foothill system also offers advantages for monitoring with optical remote sensing, featuring relatively straightforward grass + shrub + tree biophysical structure, smoothly varying topography, and low soil heterogeneity.

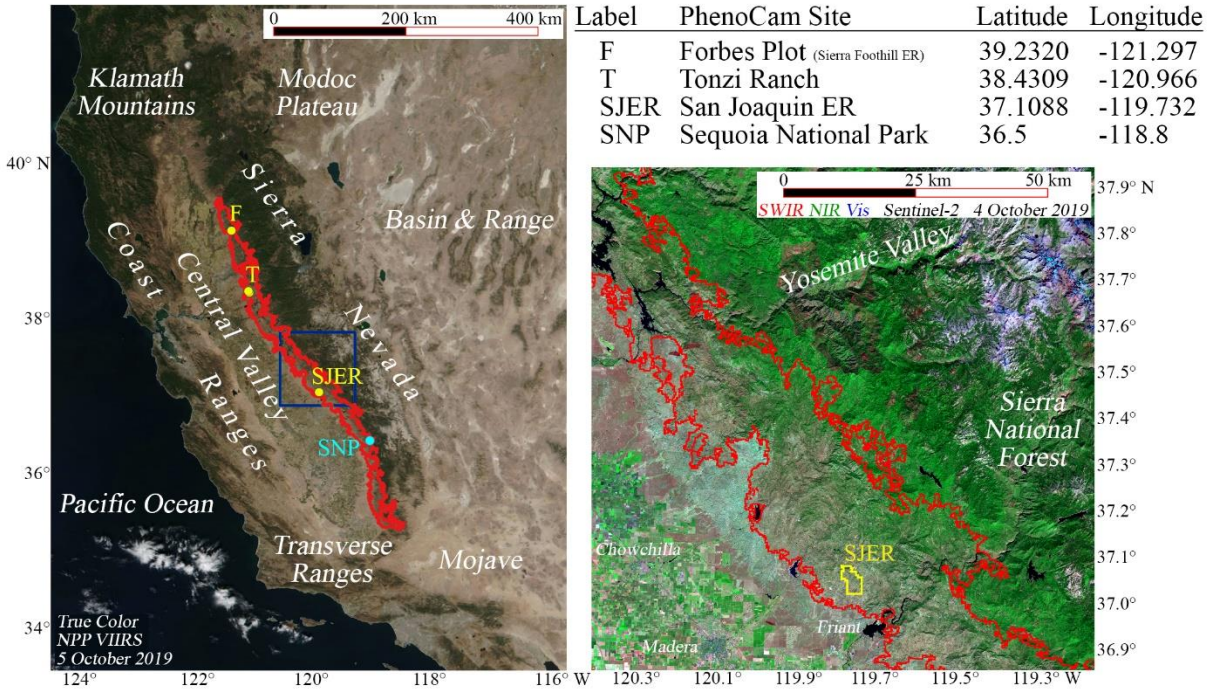

Label	PhenoCam Site	Latitude	Longitude
F	Forbes Plot (Sierra Foothill ER)	39.2320	-121.297
T	Tonzi Ranch	38.4309	-120.966
SJER	San Joaquin ER	37.1088	-119.732
SNP	Sequoia National Park	36.5	-118.8

Figure 2. Index map. Red outline shows approximate extent of Blue Oak (*Quercus douglasii*) in woodlands, savannas, and grasslands of the Sierra Nevada foothills. Yellow dots indicate PhenoCam locations used in Figures 4 and 5. Dark blue box and right panel show extent of the Sentinel-2 tile (11SKB) containing the San Joaquin Experimental Range (SJER, yellow vector), used for the single-year mapping example in Figures 6, 8a, 9 and 10. Cyan dot shows approximate location of foothill ecosystems within Sequoia National Park (SNP), site of multi-year analysis and validation example in Figures 7 and 8b.

We specifically focus on the ≈1200 km^2 area mapped by the Jepson Flora Project (Baldwin et al., 2020) as *Northern, Central, and Southern Sierra Nevada Foothills: Oak Woodlands*. The study area is comprised of a narrow (~25 km wide) band of relatively low (~200 to 600 m ASL) elevation foothills spanning over 500 km in length. The climate of the study area is classified as hot summer Mediterranean (Köppen *Csa*). The San Joaquin Experimental Range (SJER), a longstanding research station (est. 1934), is chosen as the location of our LiDAR-based validation/comparison on the basis of extensive ancillary data associated with its status as a Core Terrestrial site of the National Ecological Observatory Network (NEON). A number of deciduous and evergreen oak species occur throughout the study area, primarily including *Quercus douglasii* (blue oak), *Q. lobata* (valley oak), *Q. wislizeni* (interior live oak), and *Q. chrysolepis* (canyon live oak). Understory floristic composition is variable, with a mixture of evergreen and deciduous shrubs and annual and perennial grasses. Sequoia National Park (SNP) is a longstanding federally protected area (est. 1890). Most of the park is characterized by rugged topography, with an elevation gradient spanning over 4000 m. A diverse set of vegetation communities exist in the park. We focus on the relatively small spatial subset of SNP which

hosts blue oak woodlands, found at low elevations near the western park boundary. These woodlands are dominated by *Q. douglasii*, and also commonly include *Q. wislizeni*, *Aesculus californica* (California buckeye) and *Fraxinus dipetala* (California ash). This area was the subject of a recent study by (Das et al., 2020) which presented field evidence of drought-associated oak mortality. We focus our multi-year demonstration on this region in order to highlight a use case of potential interest to the ecological and conservation communities.

B. The mixed pixel

Relatively few individual tree canopies in the Sierra foothills have diameters exceeding the 10 m nominal Ground Instantaneous Field of View (GIFOV) of the Sentinel-2 visible through near infrared (VNIR) spectral bands, and far fewer exceed the 30 m GIFOV of Landsat-series sensors. Because the spatial scale of the objects of interest on the landscape is finer than the spatial resolution of the sensor, most pixels in these images are spatially mixed – i.e., they integrate signal from more than one object on the landscape. This phenomenon is illustrated in Figure 3. While the 30 cm resolution of the airphoto is sufficient to resolve all individual trees and most shrubs, the area integrated by most Landsat and Sentinel-2 pixels (gray squares) clearly extends beyond individual canopies. The mixed pixel is thus a fundamental characteristic of decameter resolution imagery of the Sierra foothills (and many other landscapes), suggesting the applicability of L-resolution models – and intrinsic limitations of H-resolution models – as described by (Strahler et al., 1986).

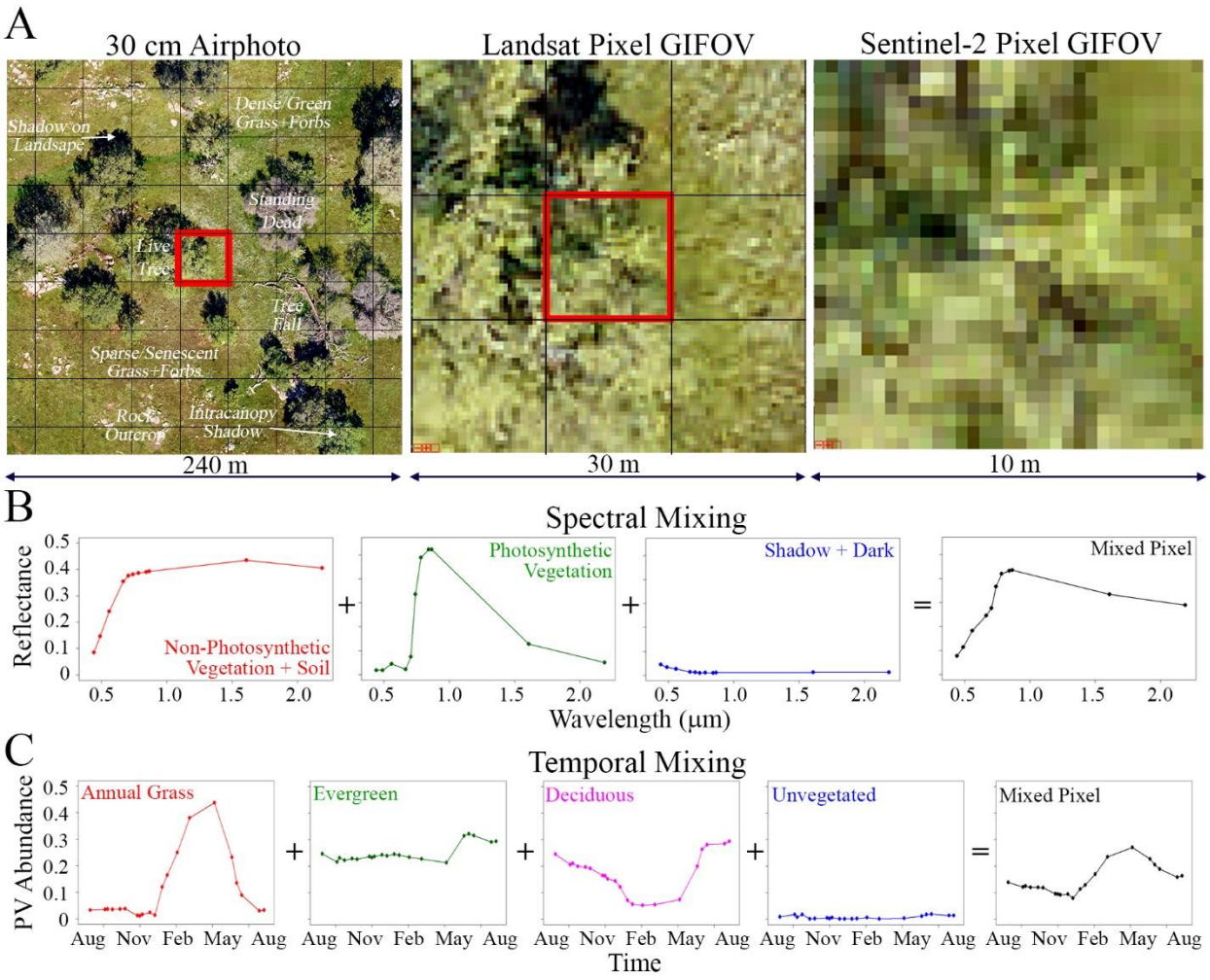

Figure 3. Subpixel mixing. A. Oak woodlands and savannas are spatially undersampled by decameter resolution sensors like Landsat and Sentinel-2. Example shown for the San Joaquin Experimental Range (SJER). When observed by low altitude airphotos (left), the landscape can be profitably segmented into discrete objects such as individual standing and fallen trees, rock outcrops, exposed soil, and grass/forb patches with varying composition. Shadowing is also evident both within plant canopies and from tall plants onto the adjacent understory. At the scale of 30 m Landsat/HLS and 10 m Sentinel-2 VNIR image time series, however, most pixels are comprised of varying mixtures of biotic and abiotic materials. B. Spectral mixture modeling estimates area abundance of spectrally distinct endmembers within each mixed pixel. C. Temporal mixture modeling simply extends this concept to the time domain, estimating subpixel area abundance of temporally distinct phenologies.

Spectral mixture analysis (SMA; (Adams et al., 1986; Gillespie, 1990; Settle and Drake, 1993)) is one well-understood approach to the mixed pixel problem for single image acquisitions. SMA optimizes the extraction of information from a multispectral image by considering the radiance (or reflectance) measured by each pixel as a linear combination of the radiance (or reflectance) of spectral endmember materials, plus error. The areal abundance of each endmember within the spatial extent of each pixel can then be estimated accurately using least squares. A fundamental assumption of spectral mixture analysis is that the landscape is comprised of a *small number of materials with distinct spectral signatures*. Linear mixing is also assumed. This concept is illustrated in Figure 3b (center row), where the reflectance of an

example mixed pixel (black curve on right) is considered to be a weighted sum of the reflectances of constituent spectral endmember reflectances (red, green and blue curves on left). SMA has been shown to accurately estimate vegetation abundance, even in sparse and multiple scattering environments like semiarid shrublands (Smith et al., 1990), exceeding the accuracy of spectral indices like NDVI in field validation exercises (Elmore et al., 2000).

In some cases, the concept of subpixel mixing can be profitably extended to the time domain. Using this approach, a landscape is considered to be comprised of a *small number of "materials" with distinct temporal signatures*. Usually, a single variable is first extracted from each image in the multispectral time series (e.g. subpixel abundance of a single material, like photosynthetic vegetation, from SMA; or a spectral index). This reduces the dimensionality of the observation space from (*t x b)* to *t*, where *t* is the number of images in the time series and *b* is the number of spectral bands in each multispectral image. The result of this step is a substantial conceptual simplification and reduction of computational load. Temporal mixing is conceptually illustrated in Figure 3c (bottom row), where an example vegetation abundance time series of a mixed pixel (black curve on right) is considered to be a linear sum of endmember vegetation phenologies (red, green, magenta and blue curves on left). This is the approach investigated in the present analysis.

Obviously, the implementation of temporal mixture analysis is considerably less straightforward than spectral mixture analysis. A number of stringent data quality and standardization requirements must be met in order for this approach to be tractable: e.g. subpixel coregistration, radiometric calibration, and consistent atmospheric correction. In addition, the formulation of the temporal mixing inverse problem is generally less well-posed than the spectral mixing inverse problem because biogeophysical parameters (e.g. vegetation abundance) can change with time in many more ways than reflectance can change with wavelength. Potential impacts of this complexity include a much higher dimensional feature space and more poorly conditioned endmember matrix for the temporal case than the spectral case. Adding to this complexity, variations in illumination and viewing geometry can introduce systematic artifacts which confound straightforward interpretation, particularly in savannas where tall trees with voluminous canopies can cast laterally extensive and seasonally variable shadows. Topography also compounds these effects. However, while these challenges complicate temporal mixture analysis, they also impact any method for satellite image time series analysis. Fortunately, decades of effort in development and implementation of preprocessing routines has succeeded in mitigating – albeit never truly eliminating – the most severe of these complications.

Materials and Methods

A. Single-year Phenology Mapping

The single-year (phenology) portion of the analysis was based on the time period July 1, 2018 through July 1, 2019. The Harmonized Landsat-Sentinel (HLS) S30 data product was the source of 30 m data, downloaded from: https://hls.gsfc.nasa.gov/. HLS data are produced free of charge and have undergone standardized radiometric, atmospheric, terrain, and BRDF correction. All available HLS images for tiles 10SFH, 10SFJ, 10SGH, 11SKA, 11SKB, 11SLA and 11SLV over the study period were downloaded and visually inspected. Images with visible cloud cover

and swath edge images with partial spatial coverage were removed. Linear spectral mixture analysis was then performed on each remaining image based on standardized global spectral endmembers from (Small, 2018). A unit sum constraint with a weight of unity was used for all instances of spectral and temporal mixture analysis. The vegetation fraction images were stacked to produce a single image time series for each tile. The images used for each tile are listed in Table S1. The single-year 30 m stacks were used for PhenoCam comparison (Figure 5), single-year example TMM (Figure 6), and investigations of spatial scaling (Figure 9), temporal aliasing (Figure 10), and cross-tile consistency (Figure 11).

10 m maps used for LiDAR comparison (Figure 8a) and spatial scaling (Figure 9) were derived from Sentinel-2 data downloaded free of charge from the Copernicus data portal: https://scihub.copernicus.eu/dhus/. Images were downloaded as Level 1C Top of Atmosphere (TOA) reflectance and processed to Level 2 Surface Reflectance using the Sen2Cor processing module available within the ESA SNAP freeware program. 20 m bands were resampled to 10 m resolution. Surface reflectance images were then unmixed to produce subpixel vegetation abundance estimates using the same globally standardized spectral endmembers referenced above. Only tile 11SKB (encompassing the SJER field site) was used for the 10 m maps. The same image dates (Table S1) were used to make the 10 m and 30 m single-year stacks.

B. Multi-year Change Mapping

The multi-year portion of the analysis was based on the time period from August 2000 through August 2019. 30 m resolution maps for the multi-year analysis were derived from Landsat 5 and 8 imagery, viewed at: https://glovis.usgs.gov/. All available August images from Path 42, Row 35 were visually examined. Level-2 surface reflectance images for all visibly cloud-free acquisitions were ordered from EarthExplorer (https://earthexplorer.usgs.gov/) and downloaded from the ESPA download hub (https://espa.cr.usgs.gov/). Although the sidelap of Path 41, Row 35 also includes much of Sequoia National Park, this tile was not included in the analysis to minimize BRDF-related uncertainty and because spatial coverage of the oak landscapes of interest is incomplete. August was chosen to optimize viewing & illumination geometry, maximize the probability that healthy winter-deciduous blue oaks would be leaf-on, and minimize the probability that summer-deciduous trees like the California Buckeye would be leaf-on. Linear spectral mixture analysis was then performed on each image based on cross-calibrated global spectral endmembers from (Sousa and Small, 2017). A unit sum constraint with a weight of unity was again used for all instances of spectral and temporal mixture analysis. The vegetation fraction images were stacked to produce a single multi-year image time series and used for the SNP analysis (Figure 7). The images used are listed in Table S2.

C. Ancillary Field and Airborne Observations

PhenoCam data were downloaded free of charge from the PhenoCam webpage: https://phenocam.sr.unh.edu/. Plots were made using 3-day maximum midday green chromatic coordinate (GCC) and standard regions of interest available on the PhenoCam website. The SJER top-of-tower PhenoCam was repositioned partway through the time series, so only images from after the repositioning (September 28, 2018 onward) were used.

The NEON Airborne Observation Platform (AOP) collected 30 cm resolution orthophotos and LiDAR at the SJER site in June 2013, and March/April 2017, 2018, and 2019. These data were downloaded free of charge from the NEON data portal (https://data.neonscience.org/home). The 1 m 2018 LiDAR canopy height model (CHM) was converted to tree presence/absence by simple thresholding. A number of thresholds were tested, and a conservative 3 m threshold was ultimately adopted. The 1 m image was then aggregated to 10 m resolution and convolved with a 9x9 pixel low-pass Gaussian blurring filter to approximate the point spread function of Sentinel-2 sensor. Because both the "deciduous perennial" and "evergreen perennial" fractions are associated with trees and shrubs, these two fractions were summed to form a "tree" fraction in the single-year dataset.

Unfortunately, healthy leaf-off deciduous oaks could not be confidently discriminated from defoliated/standing dead oaks in the 2017, 2018 and 2019 NEON AOP airphotos due to flight timing (late March to early April) occurring prior to full greenup of deciduous oaks. Validation of the single-year TMM was done by comparison to the 2018 and 2019 NEON AOP (to discriminate among grasslands, evergreen trees, and deciduous/dead trees), then cross-checked against orthophotos and meter-resolution satellite imagery available on Google Earth. Validation of the multi-year TMM was done by comparison to Google Earth imagery alone. Availability of summer validation images at SNP were limited (single image pair from 6/27/2010 and 5/31/2014), not allowing for confident assessment of the early decline + revegetation fraction.

Results

Results are presented in the following sequence. First, we leverage the PhenoCam sites to visually display the field-based time varying optical properties of representative landscapes in the study area, qualitatively connect satellite image time series to ground-based phenology observations, and compare quantitative field-based and satellite-based metrics (Subsection A). Next, we present an illustrative example of the workflow of characterization and modeling (B), followed by validation and comparison (C) of both single-year phenology mapping and multi-year change mapping. We then examine the sensitivity (D) of the resulting maps to pixel size, temporal sampling, and spatial consistency across the Sierra foothill spatial domain.

A. Relating ground and satellite observations

Initial characterization is performed using time lapse field photography from the PhenoCam program (locations shown in Figure 2). These images provide useful qualitative and quantitative information for relating time-varying surface biophysical properties to satellite image time series (Figure 4). Sites include a spatially extensive annual grassland (Forbes Plot at the Sierra Foothill Experimental Range), a deciduous blue oak woodland (Tonzi Ranch), and a mixed grassland/evergreen oak/deciduous oak/conifer landscape (SJER) (Figure 4).

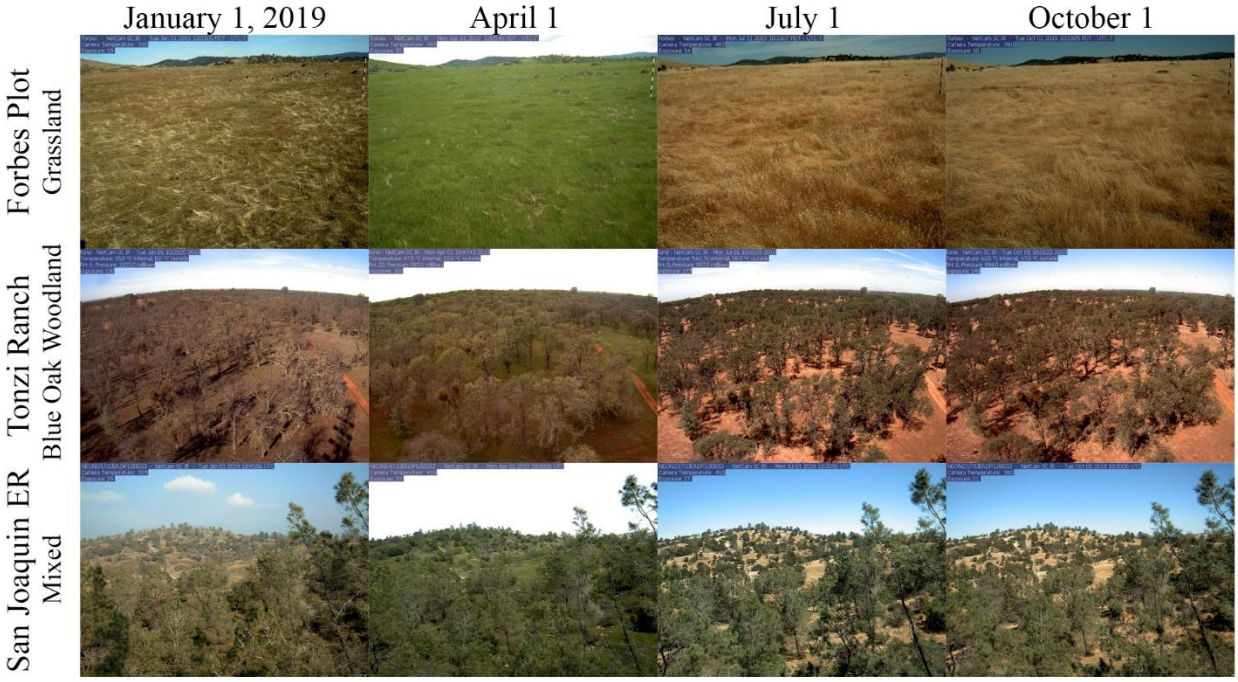

Figure 4. PhenoCam field photos. Oak density in Sierra foothill landscapes grades continuously from open, nearly treeless grasslands to closed woodlands. The PhenoCam network captures sites which span much of this range. Phenology of open grasslands (Forbes Plot at Sierra Foothill Experimental Range) is visibly different from that of oak-dominated woodlands (Tonzi Ranch). Evergreen conifers, visible in the mixed landscape of the San Joaquin Experimental Range, have yet different phenology. Typical annual cycles for each location are shown using mid-day images for each location. In areas dominated by annual grasses and deciduous oaks, maximum leaf cover (and primary production) occurs in the spring, when temperatures warm and the root zone water content is greatest. Non-native grasses senesce rapidly in late spring, but deciduous oaks (as well as some grasses, forbs, and shrubs) generally remain green through fall.

Strong seasonality in photosynthetic vegetation abundance is readily apparent at each location, but with plant types differing widely in amplitude and rate. Spatially averaged estimates for each location are shown using both ground-based and satellite-based metrics in Figure 5. Because of the differences in GCC and Fv metrics used across sensors (detailed in Materials and Methods), each plot is converted into standard scores (z-scores) by subtracting data values by the time series mean and dividing by the standard deviation. Correlation coefficients of ground-based and satellite-based time series range from 0.8 to 0.9.

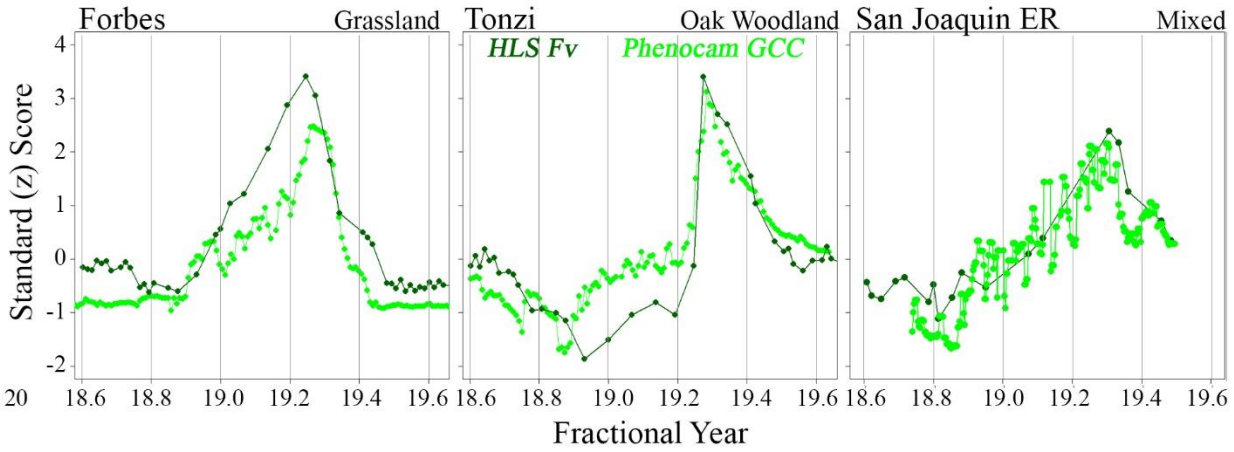

Figure 5. Phenocam versus satellite time series. The 2018-2019 water year is shown for the Forbes plot grassland (left), Tonzi Ranch blue oak woodland (center) and San Joaquin Experimental Range (right). 3-day average Green Chromatic Coordinate (GCC; lighter curve) from standard PhenoCam regions of interest is plotted with Harmonized Landsat-Sentinel (HLS) estimates of illuminated fraction of photosynthetic vegetation (Fv) from the pixels nearest the viewshed of each PhenoCam. For comparison, time series are normalized by transformation into Standard (z) Scores [i.e. $(x-\mu)/\sigma$]. Grasses show a gradual greenup throughout the winter, followed by abrupt senescence in late spring with diminishing water availability. Blue oak woodlands show loss of leaves in late fall/early winter and remain unvegetated until leaf on in spring. Evergreen/deciduous/annual landscape at SJER has a mixed phenology signal. The level of PhenoCam/HLS agreement is encouraging given differences in spatial coverage, sensing modalities and view angle. Corrlations are in the 0.8 to 0.9 range. Differences are likely due to a combination of BRDF effects and nonlinearities between the GCC and Fv metrics. The spectral mixture model also produces simultaneous estimates of two other land cover fractions (Substrate and Dark). Correlation between the Substrate fraction and PhenoCam Red Chromatic Coordinate (RCC) time series (not shown, 0.75 to 0.9) is also encouraging.

Clear differences in amplitude and timing exist among the three sites. The grass-dominated, northernmost Forbes site shows a gradual green-up throughout the winter as grass growth is enabled by winter precipitation but rate-limited by cold winter temperatures. Following the peak in early spring, the grasses senesce rapidly as water becomes limited, with a brief plateau in late spring/early summer. The blue oak woodland at the Tonzi site shows a rapid green-up in late spring as grass growth coincides with abrupt leaf-on of the deciduous oak canopy. Senescence also begins rapidly as the grass understory dries, but then slows and continues throughout the summer and into late fall/early winter, as the chlorophylls in blue oak leaves slowly degrade over the course of several months. Deciduous blue oak leaves then fall to the ground, resulting in an abrupt drop in greenness toward the end of the calendar year. Finally, the temporal signature of vegetation abundance in the mixed landscape at SJER shows less pronounced seasonality as a result of a greater abundance of evergreen oaks and conifers.

In short, the three exemplary PhenoCam sites illustrate three distinct phenologies present in the Sierra foothill oak woodland study area – annual grasses at Forbes; deciduous trees and shrubs at Tonzi; and a mixture including evergreen trees and shrubs at SJER. These phenologies can be quantified with comparable fidelity using both ground-based and satellite-based metrics. This context is invaluable for TMM implementation and interpretation, presented next.

B. Spatiotemporal Characterization & Temporal Mixture Modeling

The following methodology is based in two stages: 1) *characterization* of the dominant spatiotemporal patterns present in the image time series, and 2) *modeling* the data as a linear combination of these endmember patterns. Characterization consists of Empirical Orthogonal Function (EOF) analysis of the image time series, followed by interrogation of the associated Temporal Feature Space (TFS) to find bounding temporal endmembers (tEMs) as described by (Small, 2012). Modeling is performed by least squares. For the sake of brevity, we omit detailed discussion of the partition of variance, covariability matrices, and higher order dimensions in the current analysis. Instead we focus on the geometric structure of the low-order (Dimensions 1-3) projections of the TFS. We also focus the following portion of the analysis (Figures 6-10) on single tile spatial domains, deferring extension of the results to the remainder of the study area until Figure 11. In order to illustrate the range of potential uses of the method, both single-year and multi-year use cases are investigated.

1. Single-Year

We begin by applying a covariance-based Principal Components transform to the single-year time series. The associated low-order TFS with bounding tEM phenology time series (left) and TMM phenology map (right) are shown in Figure 6. The single-year vegetation abundance image time series is characterized by four distinct tEM phenologies located in clearly defined corners of the low-order temporal feature space: annual grasses (Ag), deciduous perennials + seasonal shadow (D), evergreen perennials (E), and unvegetated surfaces (U). Importantly, the annual cycle of subpixel photosynthetic vegetation for deciduous trees and shrubs is mimicked by the annual cycle of shadowing. This fundamental ambiguity reduces the accuracy of the deciduous fraction. The choice of Ag, D, and E single-year endmembers from the HLS spatiotemporal characterization is further reinforced by clear correspondence to the PhenoCam time series (Figure 4).

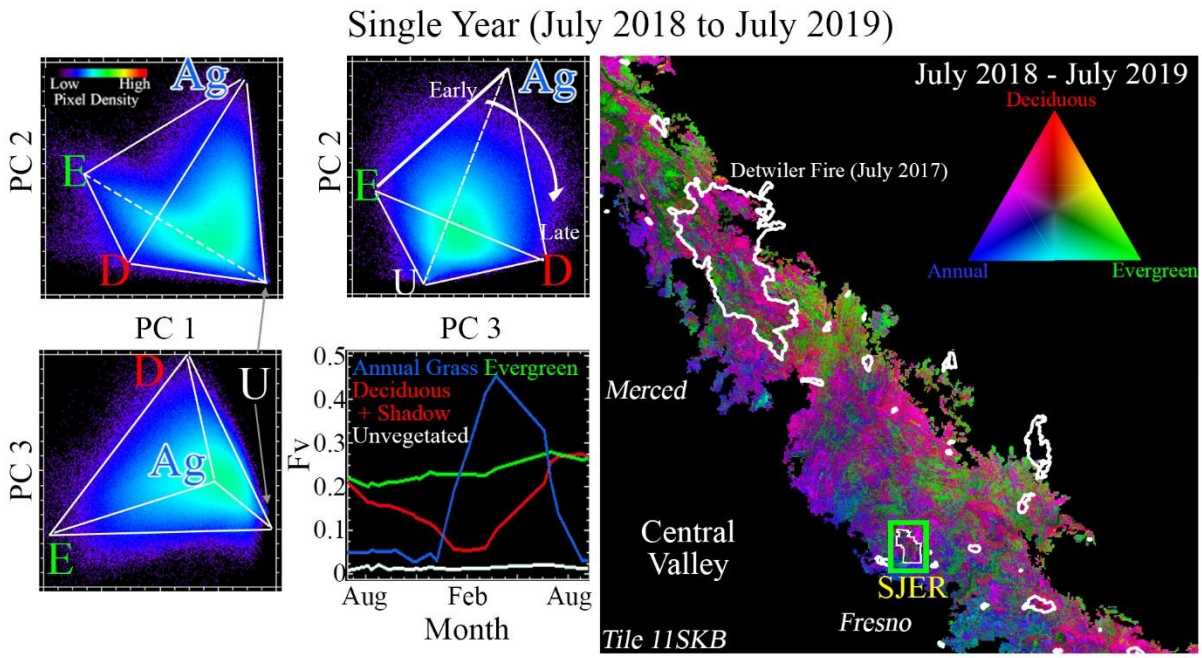

Figure 6. Single year example. The temporal feature space (TFS; left) and associated temporal mixture model (TMM; right) map are illustrated using a single year time series of vegetation abundance in tile 11SKB. The first three dimensions of the single year TFS clearly allow for discrimination between annual grasses (Ag), deciduous perennials + seasonal shadow (D), evergreen perennials (E), and unvegetated areas (U). Temporal endmembers (tEMs) representing each phenology are selected from the corners of the TFS and plotted in the lower right quadrant. These tEMs are then used to unmix the vegetation time series, generating a phenology map. The area surrounding San Joaquin Experimental Range (J; green box) is used for LiDAR comparison in Figure 8a. Fire perimeters (2015 onward) shown by white vectors.

The Ag, D, E and U tEMs bound a roughly tetrahedral mixing space, illustrated by the white lines drawn on the TFS for conceptual guidance. The TMM constructed from these tEMs represents the vegetation time series of each pixel as a linear combination of the constituent tEM phenologies. The contribution of each tEM to a pixel time series can be visualized as the Euclidean distance of that pixel from the corner of the tetrahedron corresponding to each tEM.

When displayed in geographic space, the relative contribution of each tEM generates a phenology map. This map represents the Sierra foothill landscape within tile 11SKB in terms of subpixel spatial abundance of deciduous perennials (red), evergreen perennials (green) and annual grasses (blue). Plant communities with homogenous phenologies are represented by the additive primary colors. Plant communities with intermixed phenologies correspond to areally weighted color combinations of the additive primaries. As noted above, the deciduous signal is mimicked by seasonal shadow. Despite this fundamental ambiguity, the overall spatial pattern associated with the single-year TMM is encouraging given knowledge of the landscape. The validation location (Section C) is indicated by the green box.

2. Multi-year

Another approach to analysis focuses on multi-year change rather than single-year phenology. To illustrate this analogous approach, we use the 2000-2019 August image time

series of Sequoia National Park. This time period was chosen to span the duration of the historic 2011-2017 drought as well as provide 10 years preceding the event to understand the pre-drought baseline. The corresponding TFS with bounding tEM multi-year trajectories (left) and TMM multi-year change map (right) are shown in Figure 7. A number of fires occurred in the area over the duration of the time series. Fire perimeters are shown as black vectors.

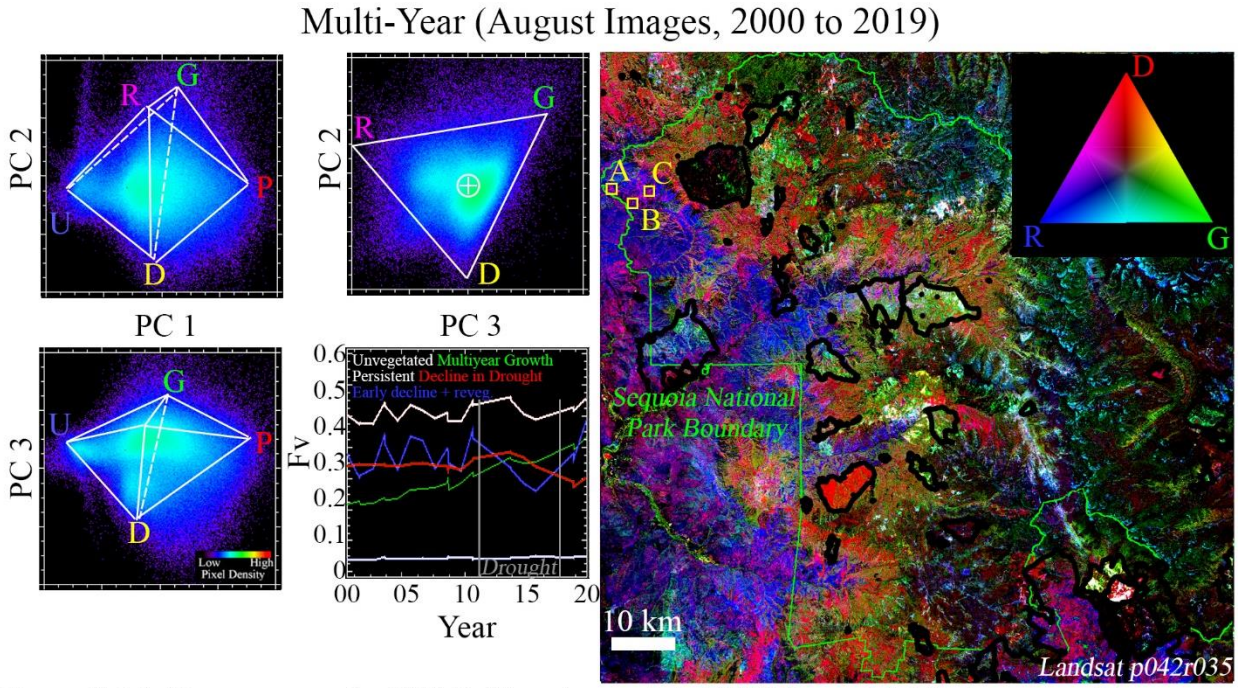

Figure 7. Multi-year example. TFS (left) and associated TMM map (right) show a multi-year change analog to the single-year phenology example from Figure 6. Model is based on a 20-year Landsat 5 and 8 time series of August vegetation abundance for Sequoia National Park and environs. Locations of example validation sites (A, B & C) shown in Figure 8b are indicated with yellow boxes. The low-order TFS forms a mixing space approximating a trigonal dihedral geometry, outlined by white lines. Temporal endmembers correspond to unvegetated (U; white), persistent (P; white), multiyear growth (G; green), decline during 2011-2017 drought (D; red), and decline in early years of drought followed by regrowth (R; blue). Beginning and ending of drought indicated by vertical gray lines. TMM shows spatial patterns corresponding to the R, D, and G tEMs. Park boundary shown with green vector and fire boundaries (1990-present) shown with black vectors.

In this case, the spatial structure of the TFS is characterized by additional complexity. Endmembers corresponding to multi-year growth (G), decline during the drought years (D) and early decline followed by revegetation (R) are observed, as well as tEMs representing unvegetated locations (U) and locations which maintained persistent August vegetation cover throughout the drought (P). Again, the TMM bounds the mixing space defined by each tEM, in this case forming a roughly trigonal dipyramidal structure (white lines).

The spatial pattern of vegetation response to drought suggests a number of hypotheses regarding the relationship between drought stress and topography. Detailed examination of landscape-scale patterns of drought response is beyond the scope of this work, but some potential paths for future work are further elaborated in the Discussion. The locations of example meter-scale validation images (Figure 8b) are shown by yellow boxes (A-C).

C. Comparison & Validation

Comparison of the single-year TMM to the 2018 NEON AOP LiDAR dataset from SJER is shown in Figure 8a. The spatial extent of the validation corresponds to the area shown in the green box in Figure 6. The resulting correlation between the Sentinel-2 derived TMM and the LiDAR-derived tree map is 0.74. The strength of the relationship is significantly improved by using the deciduous/shadow + evergreen fraction sum described in the Materials & Methods section (upper right) as opposed to a single fraction alone (lower right). This is in accord with the mixture of evergreen and deciduous trees and shrubs at the site.

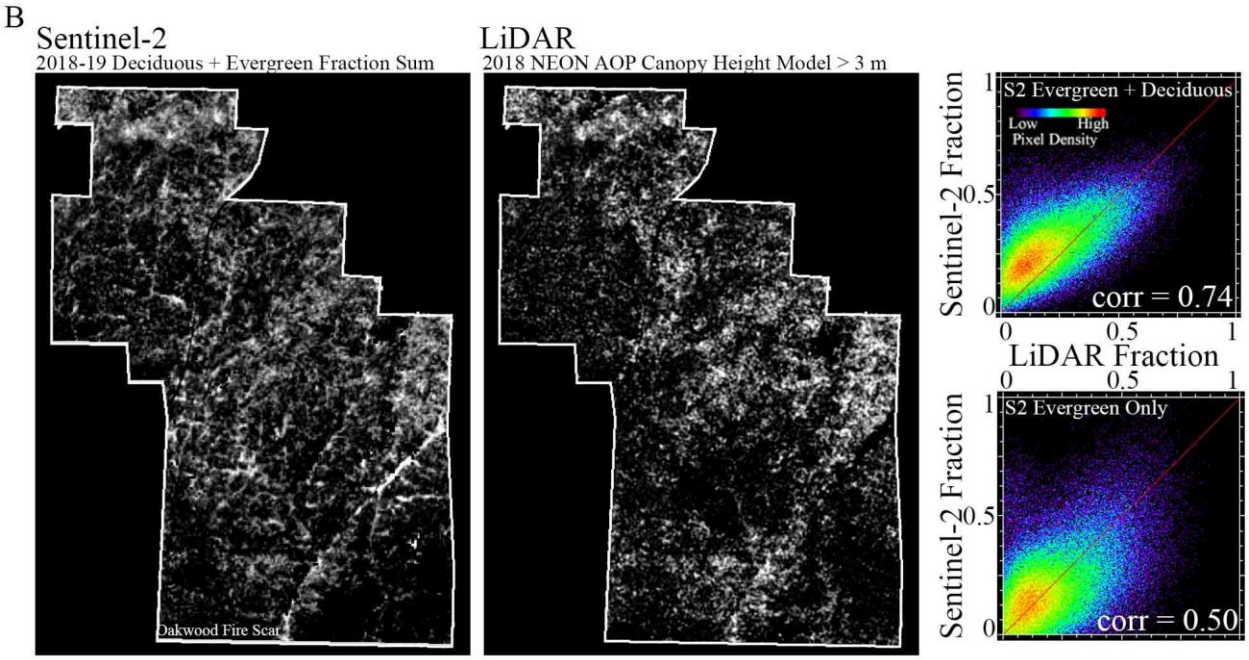

Figure 8a. Comparison of tree cover estimate to SJER LiDAR. Sentinel-2 single year evergreen + deciduous fraction sum correlates with 2018 NEON AOP LiDAR canopy height model >3 m at a level of 0.74. Sentinel-2 fractions slightly overestimate tree abundance at low fractions and underestimate tree abundance at high fractions. Correlation is substantially weaker for Sentinel-2 evergreen or deciduous fraction alone, as expected given mixed tree phenology.

Additional validation of the single-year phenology map was performed at SJER by comparing single-year phenology map fractions against sub-meter resolution airphotos and meter-resolution commercial satellite imagery. The continuous TMM was converted to a binary classification by thresholding. Annual grasslands were mapped as > 0.9 Annual tEM fraction; evergreen oak woodlands were mapped as > 0.9 Evergreen tEM fraction, and deciduous oak woodlands were mapped as > 0.9 Deciduous + Shadow tEM fraction. 34 points were randomly selected from each class and manually compared against airphotos. Classification accuracies were highest for the evergreen woodland (88%) class, with the few observed misclassifications (4 of 34) all occurring in grassland/shrubland environments near lakes and/or in swales. Accuracy for the annual grassland (85%) class was comparable, with the misclassifications (5 of 34) occurring in areas with defoliated (likely dead) tree canopies, rock outcrops, or areas with dense deciduous shrub cover. The lowest accuracy was observed for the deciduous oak class (74%). As expected, misclassifications (8 of 34) were primarily located in areas in which

topography generated a seasonal shadow signal that mimicked the deciduous vegetation time series. Some misclassifications were also observed in areas with deciduous (non-oak) shrubs, rock outcrops, swales in open grasslands, or near ponds. The associated single-year confusion matrix is shown in Table S3.

Validation of the multi-year change map was more difficult given the paucity of historic summer meter-resolution imagery and relatively constrained spatial extent of the oak woodlands within Sequoia National Park. However, sufficient imagery was available in 2010 and 2014 to provide some constraints on the Landsat based analysis. Again, the continuous TMM was converted into a discrete classification though simple thresholding. Winter deciduous and evergreen systems with no change were mapped using a rule of Persistent Green tEM fraction > 0.9. Systems showing decreased August vegetation abundance through the 2011-2017 drought were mapped by using a rule of Decrease tEM fraction > 0.9. Systems showing systematically increasing August vegetation abundance were mapped by using a rule of Decrease tEM fraction > 0.9. Systems showing early decline followed by regrowth were unable to be validated due to absence of available summer meter-resolution imagery after 2014. 34 points were randomly selected and manually investigated for each of the three classes investigated. Spatial extent of validation points was confined to the oak woodland portion of the park as mapped by (Das et al., 2020). Classification accuracy was highest for the pixels showing increased and decreased August vegetation abundance through the drought, with 91% of pixels identified correctly in each case. The misclassified points showed either no definitive change in the validation image pair or changes clearly associated with anthropogenic activity. Classification accuracy was lower for the pixels showing persistently high August vegetation abundance, with 88% of pixels showing no visible change in the validation imagery. The 4 misclassified points all showed anthropogenic landscape modification. The associated multi-year confusion matrix is shown in Table S4. Example validation image pairs for the Decrease fraction are shown in Figure 8b. Most of the observed canopy browning was found to correspond to spatially contiguous clusters (e.g. panels A and B). In some cases, even browning of individual canopies (e.g. panel C) is detected.

Taken together, the combination of comparison to LiDAR-based tree cover and visual validation of both single-year and multi-year TMMs is encouraging for the potential utility of this for retrospective analysis and prospective monitoring of Mediterranean-climate oak landscapes. However, in order for the results to be maximally generalizable, important questions of sensitivity to spatial resolution, temporal sampling, and sensitivity to spatial domain must be investigated. These factors are considered in the following section.

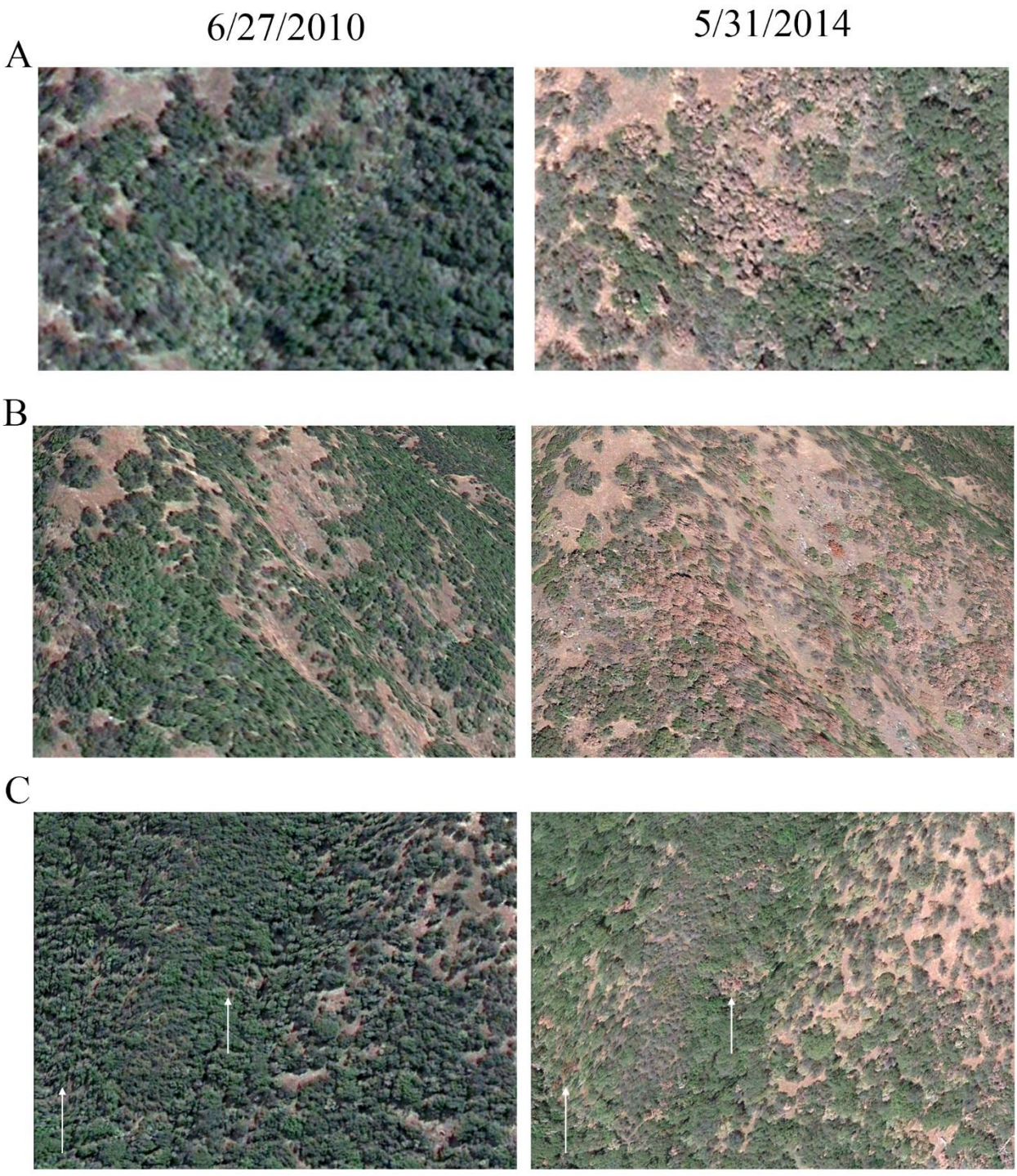

Figure 8b. Example multi-year validation. Visual comparison of meter-resolution imagery for locations indicated as decreasing through the drought. Image availability is limited, requiring the use of early summer (late May and late June) images. Despite this limitation, clear evidence of browning/defoliation is observed in 31 of the 34 areas indicated by the TMM as > 0.9 fraction of the Decrease temporal endmember. These results agree with the field measurements of (Das et al., 2020) and provide additional context in the form of spatial and temporal constraints on canopy loss.

455

D. Scaling & consistency

We first examine the effect of scaling both single-year and dual-year TMMs from 10 m to 30 m resolution. TFS characterization was done in parallel and tEMs were found to derive from the same pixels in both cases. Each image time series was unmixed using its respective temporal endmembers and fractions were compared. Results are shown in Figure 9. 10 to 30 m scaling of the single-year TMM is generally linear, with best results for deciduous and annual fractions (correlations 0.95 and 0.91), and worst results for evergreen fraction (correlation 0.78). Importantly, model misfit also scales linearly and is < 5% for > 99% of pixels.

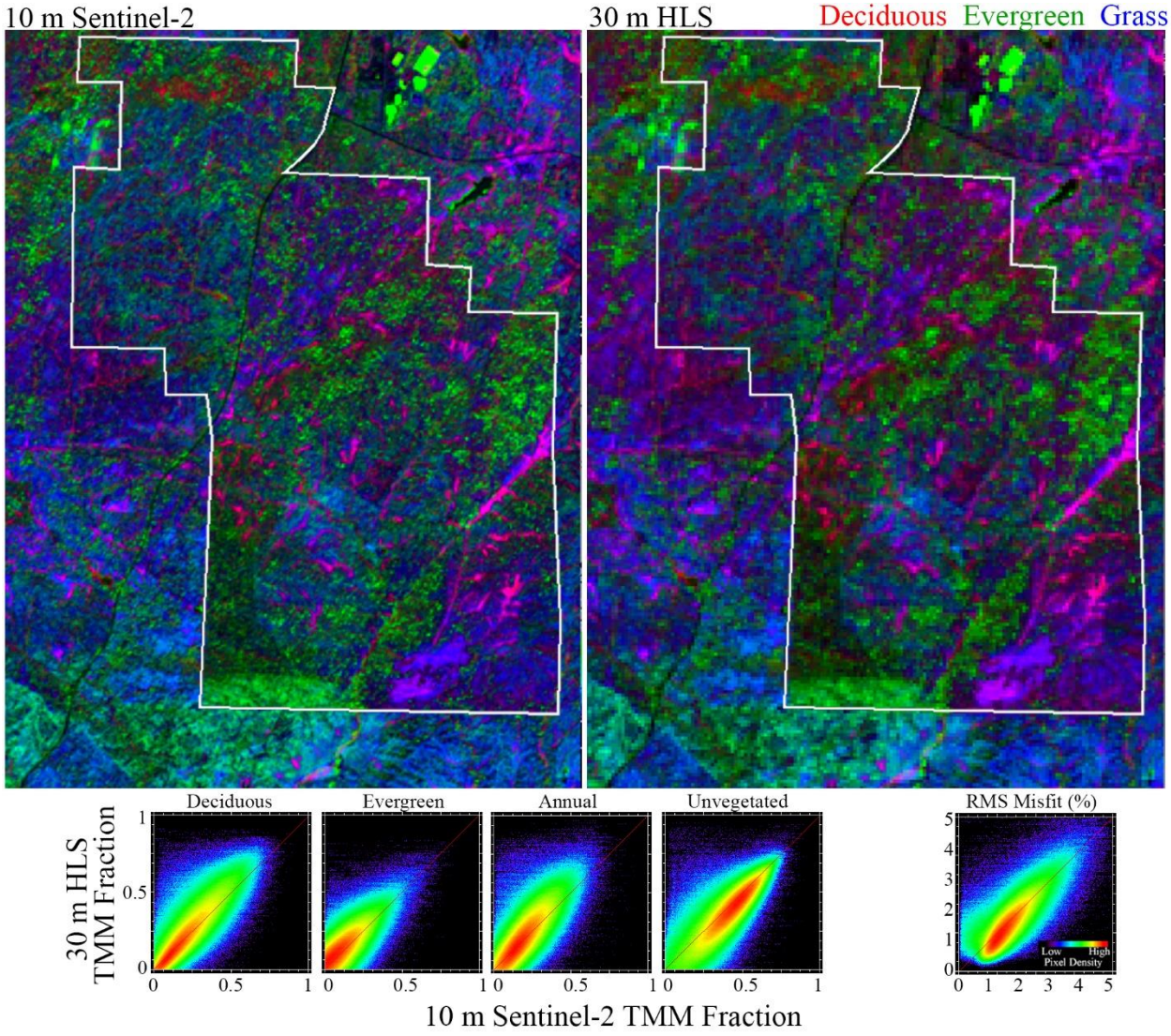

Figure 9. 10 to 30 m spatial scaling. Temporal mixture model fractions are compared for 10 m Sentinel-2 and 30 m Harmonized Landsat-Sentinel (HLS). Fractions generally scale linearly with correlations between 0.78 and 0.95. Minor bias between datasets is easily correctable with a linear transformation. This suggests that the temporal mixture model approach may be profitably applied for retrospective analysis at Landsat 4-8 spatial resolution.

We next investigate the effect of reductions in temporal sampling by systematic decimation, using the single-year 30 m TMM as our example. Figure 10 shows these results using a range of 24 images/year (full cloud-free HLS time series) down to 3 images/year. The effects on low-order TFS (A), tEMs (B), as well as linearity and bias relative to the full time series (C and D) are documented. While minor differences in the low-order TFS are noticeable in all cases, the geometric structure of the space as well as number and location of bounding tEMs are generally consistent with as few as 4 images per year. Fraction estimates show minimal bias or dispersion when subsampling at the 12 image per year level. Nonlinearity is present in the Annual fraction at 8 images per year, with even more dispersion at 6 images per year but still only minor nonlinearity. Severe nonlinearities and dispersions are observed when sampling is reduced to 4 images per year or fewer.

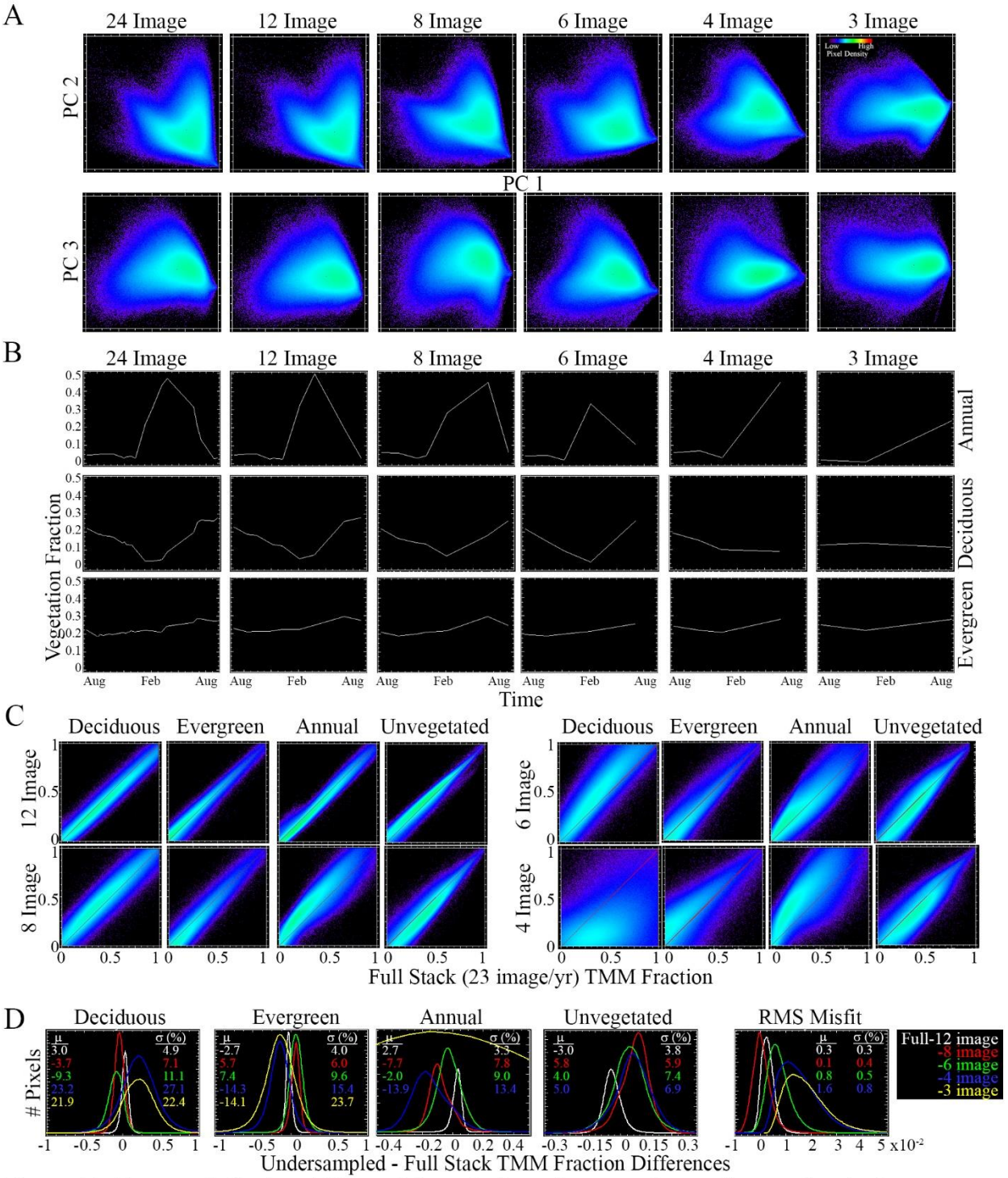

Figure 10. Temporal aliasing. Effect of degradation of temporal sampling on the single-year temporal feature space (A), temporal endmembers (B), and resulting temporal mixture model fractions (C and D) for the example HLS tile. PC 1 vs 3 topologic relations are generally retained with as few as 6 images. Fraction agreement remains linear down to the 6-image stack. Mean fraction differences are <10% for each fraction even when the temporal signal is degraded from 24 to 6 images per year. Degradation down to 4- and 3- images per year results in instability in the 4-EM inversion.

477

Finally, we investigate the consistency of the low-order TFS and tEMs across the extent of the study area. Comparable vegetation image time series are constructed for each of the 7 HLS tiles which span the Sierra foothill study area. For consistency, the same number of images in each tile are used, chosen on the basis of atmospheric clarity and maximally evenly spaced temporal sampling. The low-order TFS for each tile is rendered and bounding tEMs are selected. Results for 5 of the 7 tiles are shown in Figure 11. The two tiles not shown also conform to the pattern and are omitted for display purposes.

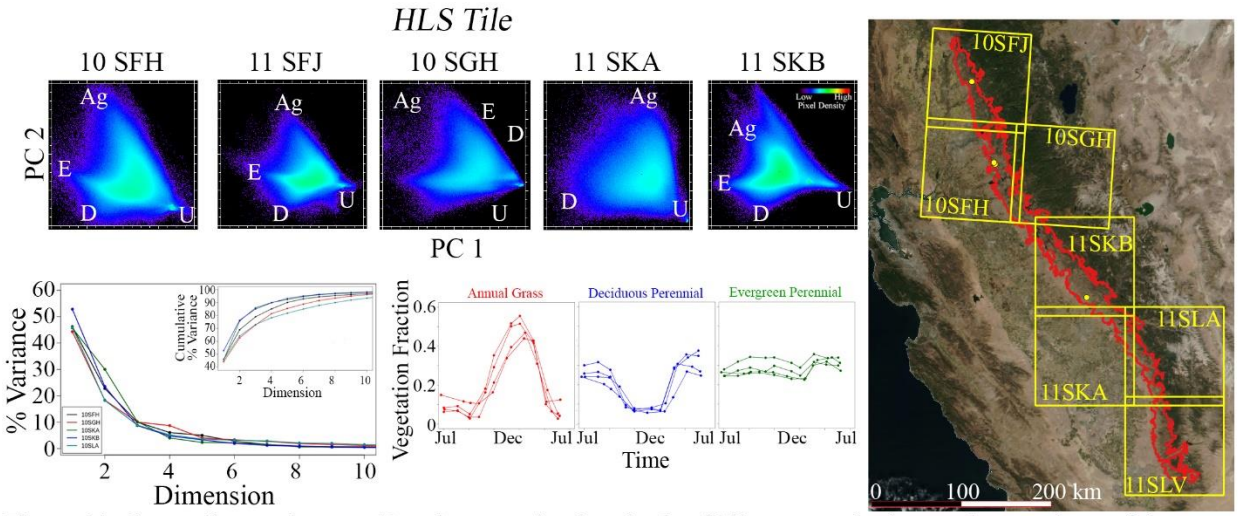

Figure 11. Cross-tile consistency. Despite spanning hundreds of kilometers, the low-order topology of the foothill oak woodland temporal feature space remains remarkably consistent across HLS tiles. Endmembers located on the PC 1 vs 2 projection represent corresponding phenological signals (evergreen, E; deciduous perennial; D, annual grass, Ag; and unvegetated, U) in each case. The sole exception is tile 11SKA, which does not show an E tEM because its spatial domain within the oak woodland mask does not include sufficient coverage of high elevations. Despite the consistency of the low-order temporal feature space, variation exists in higher dimensions, as revealed by the partition of variance (lower left). For instance, the first 2 dimensions to contain 62-75% of the overall variance in the dataset. The cumulative distribution of variance (inset) also shows this point. In some tiles (e.g. 10SFH), 90% of data variance is contained in the first 4 dimensions; other tiles (e.g. 10SLA) require as many as 10 dimensions to capture 90% of data variance. Tile 11SLA and 11SLV are not shown for brevity.

The results of the multi-tile experiment confirm that similar low-order TFS geometry and tEMs clearly characterize all but one of the tiles. The tile comprising the exception (11SKA) does not show a clear evergreen tEM. The absence of this tEM is consistent with its relatively minimal spatial extent within the Sierra foothill zone and nearly complete absence of pixels at higher elevations which comprise the bulk of the evergreeen corner of the feature space. The observed consistency in TFS structure, tEM time series, and data dimensionality is taken as further support for the validity of the inferences made in this work across the 500 km spatial extent of the Sierra foothill grassland – oak savanna – oak woodland ecosystem.

Discussion

A. Benefits of the methodology

The methodology presented here possesses a number of benefits for the analysis and monitoring of Mediterranean-climate oak landscapes. Among the primary features are conceptual simplicity, explainability, and parsimony. These features arise from the linearity of the mixing equations and compact geometric interpretation of the TFS and TMM. However, by explicitly accommodating the structure of the TFS, the approach is designed such that maximum explanatory power is also retained. Once tEMs are selected, the only tunable parameter is the weight associated with the unit sum constraint.

In addition, the single-year tEMs have clear biophysical interpretation. The phenology signatures present in the PhenoCam time series, HLS time series from single pixels in PhenoCam viewsheds, and independently derived landscape-scale tEMs derived from TFS structure provide mutually reinforcing signals. We interpret this consistency as strong evidence that: 1) the tEMs selected here are stable features of the Sierra foothill spatial domain, 2) the tEMs accurately represent characteristic vegetation phenologies of common plant types, and 3) multispectral satellite time series of the study area can be well described by these tEMs. Incidentally, while previous studies have compared PhenoCam spectral indices to MODIS/VIIRS spectral indices (Liu et al., 2017; Richardson et al., 2018; Zhang et al., 2018), to our knowledge this is the first published comparison of PhenoCam data against vegetation fraction estimated using spectral mixture analysis of near-nadir decameter satellite imagery.

At least as important as the features discussed above, however, are the benefits of the robustness and portability of the approach. Supporting observations include linear 10 to 30 m scaling (Figure 9), insensitivity to (modest) temporal degradation (Figure 10), and insensitivity to changes in spatial extent across the study domain (Figure 11). As a further practical consideration, the approach is not computationally onerous (< 1 min unmixing time per tile on laptop computer for 4 EM single-year time series) and does not require extensive training data.

The strengths discussed above suggest that the potential for retrospective analysis and prospective monitoring across the entire range of the California Oak woodland/savanna system using this approach is considerable. A similar model could also be easily adopted for analysis of other biophysically similar Mediterranean-climate oak landscapes in the Mediterranean basin. Finally, the considerations described above are important benefits relative to deep learning approaches which, while powerful, often lack one or more of these features. Ultimately, the most effective approach to monitoring oak woodland systems is likely a multifaceted approach using a combination of TMM analysis of multitemporal decameter imagery, in conjunction with directed object-oriented and deep learning analyses using aerial surveys and meter resolution satellite imagery – complemented with extensive field validation.

B. Limitations

Effects due to observational geometry and atmospheric conditions are fundamental limitations that must be considered by all satellite image time series analysis approaches. As noted throughout this analysis, the most prominent way this factors into the model presented here

is the ambiguity between deciduous vegetation and seasonal shadow. Ongoing improvements in ancillary observations (e.g. digital elevation models, atmospheric constraints) and preprocessing algorithms mitigate the severity of these problems, but are unlikely to ever fully eliminate them – and may introduce additional unintended artifacts. Fortunately, topographic/BRDF effects are relatively minor in the Sierra foothills due to gentle topography – but are much more severe at higher elevations, particularly in glacially scoured landscapes and escarpments. Data loss during times of spatially extensive cloud cover (e.g. winter in the Sierra Foothills) remains an unavoidable limitation. This is particularly problematic for retrospective studies which are not able to leverage recent advances capability with respect to shortened revisit time.

Phenology-based studies relying on vegetation abundance (or any "greenness" metric) are fundamentally limited by the phenomenon of phenological mimicking. Because the operative signal is derived from temporal variations in photosynthetic vegetation, in many landscapes it is probable that several plant species may possess annual cycles which are indistinct using this metric alone. We caution against overinterpretation of the results of such analyses, including the analysis we demonstrate here. Phenological variation measured in this way may be driven by a number of factors. Careful consideration and field validation (wherever possible) is necessary before confident interpretation of such results as supporting or refuting a given ecological hypothesis. However, we also note that the limitations described above apply to any comparable analysis approach based on multispectral satellite imagery.

A further set of limitations applies to the TMM methodology in particular. One important assumption underlying this approach is the linear mixing assumption. While this assumption holds true for the *spectral mixing* case in a wide range of terrestrial environments, the testing of this assumption has been less thorough for the *temporal mixing* case. Two pieces of supporting evidence for the validity of linear temporal mixing assumption in this study are: 1) the presence of corners and edges in the TFS, suggesting binary linear mixing lines, and 2) the linearity of fraction estimate scaling from 10 to 30 m resolution. However, the observed binary mixing lines are admittedly more ambiguous in the temporal mixing case than the spectral mixing case, and some deviation from the 1:1 line is observed in the spatial scaling investigation. This fundamental question, as well as further considerations about model performance such as the conditioning of the inversion and higher-order complexity due to large non-noise data dimensionality, are interesting and potentially informative. We defer detailed investigation of these factors to a future study.

C. Directions for future work

One potential avenue to extend this methodology is the incorporation of time series observations beyond decameter multispectral images. A recent and ongoing surge in observational capacity provides a number of avenues of potential development. Measurements with higher spatial resolution and/or shorter revisit time (e.g. Planet) might be used to improve measurement density – if critical data quality metrics such as subpixel geolocation and science-grade radiometry are capable of consistently being met. In addition, time series provided by orbital hyperspectral sensors could provide narrowband absorption characteristics at each time step, allowing for more refined biophysical interpretation of the spectral metric used beyond areal photosynthetic vegetation abundance. Landscape partitioning and/or object based analysis using spatially extensive LiDAR could provide further constraints to provide context and improve a multispectral-only approach for prospective monitoring. In spite of these important and exciting advances, however, a focus on multispectral observations is still warranted. At minimum, those workers interested in long-baseline landscape change requiring retrospective analysis will fundamentally be constrained by past data availability.

Another potential direction for future work is in the application of the methodology to pressing questions in ecology and land management. For instance, a regional-scale ecological analysis of the response of oak woodlands to recent climatic events like the 2011-2017 drought could easily be implemented, and a monitoring system could be developed. Fire agencies, land managers and fire ecologists could use this approach to observe spatial patterns of vegetation recovery in burn scars and potentially constrain models of regrowth and post-fire hydrology. Range managers and rangeland scientists could use the approach to monitor range conditions and potentially predict spatial patterns of forage abundance. Finally, the question of phenologic complexity of a mixed pixel and temporal dimensionality of a landscape may ultimately provide novel insight into the ability to estimate spatial patterns of biodiversity.

Conclusions

The purpose of this work is to introduce Temporal Mixture Modeling (TMM) for the mapping and monitoring of Mediterranean-climate oak landscapes, focusing on the California Sierra foothill oak system. On the basis of both PhenoCam time lapse field photography and Temporal Feature Space (TFS) geometry, the dominant single-year phenologies in these landscapes are found to be Annual Grasses, Deciduous Perennials, and Evergreen Perennials. Tree cover fractions were observed to correlate at the 0.74 level to LiDAR-derived tree (>3 m) estimates from the 2018 NEON AOP aerial survey at San Joaquin Experimental Range. Further visual validation of the TMM-derived phenology map against orthophotos found the accuracy of fraction estimates to range from 74% (deciduous perennials) to 88% (evergreen perennials). A multi-year time series of August imagery (2000 through 2019) was also analyzed to investigate the effect of the historic 2011-2017 drought. The dominant multi-year phenologies were found to be: 1) unvegetated, 2) persistently vegetated, 3) growth throughout drought, 4) decrease throughout drought, and 5) early decrease followed by revegetation. Validation of multi-year change was challenging due to sparse availability of meter-resolution summer imagery, but a 2010 vs 2014 image pair allowed for assessment of behavior in the first half of the drought. When continuous fraction estimates were converted to discrete classification using a threshold of

0.9, Accuracy of the persistent evergreen fraction was 88% and of the drought-associated decline fraction was 91%. Spatial scaling from 10 m (Sentinel-2 VNIR) to 30 m (HLS and Landsat) was found to be generally linear with correlations in the 0.78 to 0.95 range. Loss of fidelity due to diminished temporal sampling was simulated and fractions were found to be scale linearly with as few as 6 observations per year. TFS and tEM consistency were found to be stable across the HLS tiles representing the California foothill oak spatial domain. Taken together, these results suggest that TMMs may provide a parsimonious, accurate, and scalable framework with which to consider the spatiotemporal analysis of Mediterranean-climate oak woodlands.

Acknowledgements

D. Sousa was funded by a postdoctoral fellowship from the La Kretz Research Center at Sedgwick Reserve.

References

Adams, J.B., Smith, M.O., Johnson, P.E., 1986. Spectral mixture modeling: A new analysis of rock and soil types at the Viking Lander 1 Site. J. Geophys. Res. Solid Earth 91, 8098–8112. https://doi.org/10.1029/JB091iB08p08098

Allen-Diaz, B., Standiford, R., Jackson, R., 2007. Oak woodlands and forests, in: Barbour, M., Keeler-Wolf, T., Schoenherr, A. (Eds.), Terrestrial Vegetation of California. University of California Press, Berkeley, California, pp. 313–338.

Asner, G.P., Brodrick, P.G., Anderson, C.B., Vaughn, N., Knapp, D.E., Martin, R.E., 2016. Progressive forest canopy water loss during the 2012–2015 California drought. Proc. Natl. Acad. Sci. 113, E249–E255. https://doi.org/10.1073/pnas.1523397113

Baldwin, B., Keil, D., Markos, S., Mishler, B., Patterson, R., Rosatti, T., Wilken, D. (Eds.), 2020. Jepson Flora Project.

Baldwin, B.G., 2014. Origins of Plant Diversity in the California Floristic Province. Annu. Rev. Ecol. Evol. Syst. 45, 347–369. https://doi.org/10.1146/annurev-ecolsys-110512-135847

Berberoglu, S., Akin, A., 2009. Assessing different remote sensing techniques to detect land use/cover changes in the eastern Mediterranean. Int. J. Appl. Earth Obs. Geoinformation 11, 46–53. https://doi.org/10.1016/j.jag.2008.06.002

Berger, M., Moreno, J., Johannessen, J.A., Levelt, P.F., Hanssen, R.F., 2012. ESA's sentinel missions in support of Earth system science. Remote Sens. Environ. 120, 84–90.

Bogan, S.A., Antonarakis, A.S., Moorcroft, P.R., 2019. Imaging spectrometry-derived estimates of regional ecosystem composition for the Sierra Nevada, California. Remote Sens. Environ. 228, 14–30. https://doi.org/10.1016/j.rse.2019.03.031

California Department of Fish and Wildlife (CDFW), 2014. California Wildlife Habitat Relationships, Version 9.0 [WWW Document]. URL https://wildlife.ca.gov/Data/CWHR (accessed 1.9.20).

Cameron, D.R., Marty, J., Holland, R.F., 2014. Whither the Rangeland?: Protection and Conversion in California's Rangeland Ecosystems. PLOS ONE 9, e103468. https://doi.org/10.1371/journal.pone.0103468

Chander, G., Markham, B.L., Helder, D.L., 2009. Summary of current radiometric calibration coefficients for Landsat MSS, TM, ETM+, and EO-1 ALI sensors. Remote Sens. Environ. 113, 893–903.

651 Chi, J., Kim, H.-C., Kang, S.-H., 2016. Machine learning-based temporal mixture analysis of
652 hypertemporal Antarctic sea ice data. Remote Sens. Lett. 7, 190–199.
653 https://doi.org/10.1080/2150704X.2015.1121300
654 Claverie, M., Ju, J., Masek, J.G., Dungan, J.L., Vermote, E.F., Roger, J.-C., Skakun, S.V.,
655 Justice, C., 2018. The Harmonized Landsat and Sentinel-2 surface reflectance data set.
656 Remote Sens. Environ. 219, 145–161.
657 Das, A.J., Ampersee, N.J., Pfaff, A.H., Stephenson, N.L., Swiecki, T.J., Bernhardt, E.A.,
658 Haggerty, P.K., Nydick, K.R., 2020. TREE MORTALITY IN BLUE OAK
659 WOODLAND DURING EXTREME DROUGHT IN SEQUOIA NATIONAL PARK,
660 CALIFORNIA. Madroño 66, 164–175. https://doi.org/10.3120/0024-9637-66.4.164
661 Davis, F., Baldocchi, D., Tyler, C., 2016. Chapter 25: Oak Woodlands, in: Ecosystems of
662 California. University of California Press, Oakland, CA, pp. 509–529.
663 Davis, F., Borchert, M., 2006. Central coast bioregion, in: Sugihara, N., Van Wagtendonk, J.,
664 Fites-Kaufman, J., Shaffer, K., Thode, A. (Eds.), Fire in California's Ecosystems.
665 University of California Press, Berkeley, California, pp. 321–349.
666 Drusch, M., Del Bello, U., Carlier, S., Colin, O., Fernandez, V., Gascon, F., Hoersch, B., Isola,
667 C., Laberinti, P., Martimort, P., 2012. Sentinel-2: ESA's optical high-resolution mission
668 for GMES operational services. Remote Sens. Environ. 120, 25–36.
669 Elmore, A.J., Mustard, J.F., Manning, S.J., Lobell, D.B., 2000. Quantifying Vegetation Change
670 in Semiarid Environments: Precision and Accuracy of Spectral Mixture Analysis and the
671 Normalized Difference Vegetation Index. Remote Sens. Environ. 73, 87–102.
672 https://doi.org/10.1016/S0034-4257(00)00100-0
673 Fricker, G.A., Ventura, J.D., Wolf, J.A., North, M.P., Davis, F.W., Franklin, J., 2019. A
674 Convolutional Neural Network Classifier Identifies Tree Species in Mixed-Conifer Forest
675 from Hyperspectral Imagery. Remote Sens. 11, 2326. https://doi.org/10.3390/rs11192326
676 Gaman, T., Firman, J., 2006. Oaks 2040: The Status and Future of Oaks in California. California
677 Oak Foundation.
678 Gillespie, A., 1990. Interpretation of residual images: spectral mixture analysis of AVIRIS
679 images, Owens Valley, California, in: Proc. Second Airborne Visible/Infrared Imaging
680 Spectrometer (AVIRIS) Workshop. NASA, Pasadena, California, pp. 243–270.
681 Guisti, G., Scott, T., Garrison, B., 1996. Oak woodland wildlife ecology and habitat
682 relationships, in: Guidelines for Managing California's Hardwood Rangelands,
683 Agriculture and Natural Resources. University of California Division of Agriculture and
684 Natural Resources, Berkeley, CA.
685 Gunning, D., 2017. Explainable artificial intelligence (XAI), Defense Advanced Research
686 Projects Agency (DARPA) Program Update.
687 Jain, M., Mondal, P., DeFries, R.S., Small, C., Galford, G.L., 2013. Mapping cropping intensity
688 of smallholder farms: A comparison of methods using multiple sensors. Remote Sens.
689 Environ. 134, 210–223. https://doi.org/10.1016/j.rse.2013.02.029
690 Klausmeyer, K.R., Shaw, M.R., 2009. Climate Change, Habitat Loss, Protected Areas and the
691 Climate Adaptation Potential of Species in Mediterranean Ecosystems Worldwide. PLOS
692 ONE 4, e6392. https://doi.org/10.1371/journal.pone.0006392
693 Koltunov, A., Ramirez, C.M., Ustin, S.L., Slaton, M., Haunreiter, E., 2019. eDaRT: The
694 Ecosystem Disturbance and Recovery Tracker system for monitoring landscape
695 disturbances and their cumulative effects. Remote Sens. Environ. 111482.
696 https://doi.org/10.1016/j.rse.2019.111482

Li, W., Wu, C., 2014. Phenology-based temporal mixture analysis for estimating large-scale impervious surface distributions. Int. J. Remote Sens. 35, 779–795. https://doi.org/10.1080/01431161.2013.873147

Liu, Y., Hill, M.J., Zhang, X., Wang, Z., Richardson, A.D., Hufkens, K., Filippa, G., Baldocchi, D.D., Ma, S., Verfaillie, J., Schaaf, C.B., 2017. Using data from Landsat, MODIS, VIIRS and PhenoCams to monitor the phenology of California oak/grass savanna and open grassland across spatial scales. Agric. For. Meteorol. 237–238, 311–325. https://doi.org/10.1016/j.agrformet.2017.02.026

Loarie, S.R., Carter, B.E., Hayhoe, K., McMahon, S., Moe, R., Knight, C.A., Ackerly, D.D., 2008. Climate Change and the Future of California's Endemic Flora. PLOS ONE 3, e2502. https://doi.org/10.1371/journal.pone.0002502

Lobell, D.B., Asner, G.P., 2004. Cropland distributions from temporal unmixing of MODIS data. Remote Sens. Environ. 93, 412–422.

Marañón, T., Marañón, T., Pugnaire, F.I., Callaway, R.M., 2009. Mediterranean-climate oak savannas: the interplay between abiotic environment and species interactions.

Mensing, S., 2006. The history of oak woodlands in California, part II: the native American and historic period.

Miller, J.D., Safford, H.D., Crimmins, M., Thode, A.E., 2009. Quantitative evidence for increasing forest fire severity in the Sierra Nevada and southern Cascade Mountains, California and Nevada, USA. Ecosystems 12, 16–32.

Miraglio, T., Adeline, K., Huesca, M., Ustin, S., Briottet, X., 2020. Monitoring LAI, Chlorophylls, and Carotenoids Content of a Woodland Savanna Using Hyperspectral Imagery and 3D Radiative Transfer Modeling. Remote Sens. 12, 28. https://doi.org/10.3390/rs12010028

Myers, N., Mittermeier, R.A., Mittermeier, C.G., Fonseca, G.A.B. da, Kent, J., 2000. Biodiversity hotspots for conservation priorities. Nature 403, 853–858. https://doi.org/10.1038/35002501

Navarro, A., Catalao, J., Calvao, J., 2019. Assessing the Use of Sentinel-2 Time Series Data for Monitoring Cork Oak Decline in Portugal. Remote Sens. 11, 2515. https://doi.org/10.3390/rs11212515

Pavlik, B., Muick, P., Johnson, S., 1993. Oaks of California. Cachuma Press, Los Olivos, CA.

Piwowar, J.M., Peddle, D.R., LeDrew, E.F., 1998. Temporal mixture analysis of arctic sea ice imagery: a new approach for monitoring environmental change. Remote Sens. Environ. 63, 195–207.

Quarmby, N.A., 1992. Towards continental scale crop area estimation. Int. J. Remote Sens. 13, 981–989. https://doi.org/10.1080/01431169208904172

Quarmby, N.A., Townshend, J.R.G., Settle, J.J., White, K.H., Milnes, M., Hindle, T.L., Silleos, N., 1992. Linear mixture modelling applied to AVHRR data for crop area estimation. Int. J. Remote Sens. 13, 415–425. https://doi.org/10.1080/01431169208904046

Recanatesi, F., Giuliani, C., Ripa, M.N., 2018. Monitoring Mediterranean Oak Decline in a Peri-Urban Protected Area Using the NDVI and Sentinel-2 Images: The Case Study of Castelporziano State Natural Reserve. Sustainability 10, 3308. https://doi.org/10.3390/su10093308

Richardson, A.D., Hufkens, K., Milliman, T., Frolking, S., 2018. Intercomparison of phenological transition dates derived from the PhenoCam Dataset V1.0 and MODIS satellite remote sensing. Sci. Rep. 8, 1–12. https://doi.org/10.1038/s41598-018-23804-6

743 Settle, J.J., Drake, N.A., 1993. Linear mixing and the estimation of ground cover proportions.
744 Int. J. Remote Sens. 14, 1159–1177. https://doi.org/10.1080/01431169308904402
745 Small, C., 2018. Multisource imaging of urban growth and infrastructure using Landsat, Sentinel
746 and SRTM, in: NASA Landsat-Sentinel Science Team Meeting. Rockville, MD.
747 Small, C., 2012. Spatiotemporal dimensionality and Time-Space characterization of
748 multitemporal imagery. Remote Sens. Environ. 124, 793–809.
749 Small, C., Sousa, D., 2019. Spatiotemporal Characterization of Mangrove Phenology and
750 Disturbance Response: The Bangladesh Sundarban. Remote Sens. 11, 2063.
751 https://doi.org/10.3390/rs11172063
752 Smith, M.O., Ustin, S.L., Adams, J.B., Gillespie, A.R., 1990. Vegetation in deserts: I. A regional
753 measure of abundance from multispectral images. Remote Sens. Environ. 31, 1–26.
754 https://doi.org/10.1016/0034-4257(90)90074-V
755 Sousa, D., Small, C., 2019. Mapping and Monitoring Rice Agriculture with Multisensor
756 Temporal Mixture Models. Remote Sens. 11, 181. https://doi.org/10.3390/rs11020181
757 Sousa, D., Small, C., 2017. Global cross-calibration of Landsat spectral mixture models. Remote
758 Sens. Environ. 192, 139–149. https://doi.org/10.1016/j.rse.2017.01.033
759 Sousa, D., Small, C., Spalton, A., Kwarteng, A., 2019. Coupled Spatiotemporal Characterization
760 of Monsoon Cloud Cover and Vegetation Phenology. Remote Sens. 11, 1203.
761 https://doi.org/10.3390/rs11101203
762 Storey, J., Choate, M., Lee, K., 2014. Landsat 8 Operational Land Imager on-orbit geometric
763 calibration and performance. Remote Sens. 6, 11127–11152.
764 Strahler, A.H., Woodcock, C.E., Smith, J.A., 1986. On the nature of models in remote sensing.
765 Remote Sens. Environ. 20, 121–139.
766 Swatantran, A., Dubayah, R., Roberts, D., Hofton, M., Blair, J.B., 2011. Mapping biomass and
767 stress in the Sierra Nevada using lidar and hyperspectral data fusion. Remote Sens.
768 Environ., DESDynI VEG-3D Special Issue 115, 2917–2930.
769 https://doi.org/10.1016/j.rse.2010.08.027
770 Swiecki, T.J., Bernhardt, E.A., Arnold, R.A., 1997. The California Oak Disease and Arthropod
771 (CODA) Database. Pillsbury Norman H Verner Jared Tietje William Tech. Coord. 1997
772 Proc. Symp. Oak Woodl. Ecol. Manag. Urban Interface Issues 19–22 March 1996 San
773 Luis Obispo CA Gen Tech Rep PSW-GTR-160 Albany CA Pac. Southwest Res. Stn. For.
774 Serv. US Dep. Agric. P 543-552 160.
775 Tyler, C.M., Kuhn, B., Davis, F.W., 2006. Demography and Recruitment Limitations of Three
776 Oak Species in California. Q. Rev. Biol. 81, 127–152. https://doi.org/10.1086/506025
777 Verbesselt, J., Hyndman, R., Newnham, G., Culvenor, D., 2010. Detecting trend and seasonal
778 changes in satellite image time series. Remote Sens. Environ. 114, 106–115.
779 https://doi.org/10.1016/j.rse.2009.08.014
780 Vermote, E., Roger, J.-C., Franch, B., Skakun, S., 2018. LaSRC (Land Surface Reflectance
781 Code): Overview, application and validation using MODIS, VIIRS, LANDSAT and
782 Sentinel 2 data's, in: IGARSS 2018-2018 IEEE International Geoscience and Remote
783 Sensing Symposium. IEEE, pp. 8173–8176.
784 Vermote, E., Saleous, N., 2007. LEDAPS surface reflectance product description. Coll. Park
785 Univ. Md.
786 Woodcock, C.E., Loveland, T.R., Herold, M., Bauer, M.E., 2019. Transitioning from change
787 detection to monitoring with remote sensing: A paradigm shift. Remote Sens. Environ.
788 111558. https://doi.org/10.1016/j.rse.2019.111558

Wulder, M.A., Masek, J.G., Cohen, W.B., Loveland, T.R., Woodcock, C.E., 2012. Opening the archive: How free data has enabled the science and monitoring promise of Landsat. Remote Sens. Environ., Landsat Legacy Special Issue 122, 2–10. https://doi.org/10.1016/j.rse.2012.01.010

Yang, F., Matsushita, B., Fukushima, T., Yang, W., 2012. Temporal mixture analysis for estimating impervious surface area from multi-temporal MODIS NDVI data in Japan. ISPRS J. Photogramm. Remote Sens. 72, 90–98. https://doi.org/10.1016/j.isprsjprs.2012.05.016

Zhang, X., Jayavelu, S., Liu, L., Friedl, M.A., Henebry, G.M., Liu, Y., Schaaf, C.B., Richardson, A.D., Gray, J., 2018. Evaluation of land surface phenology from VIIRS data using time series of PhenoCam imagery. Agric. For. Meteorol. 256–257, 137–149. https://doi.org/10.1016/j.agrformet.2018.03.003

Tables S1 through S4

Click here to download Table: SousaDavis_SierraFoothillOakTMM_Tables.docx

Table S1. Image dates from each of the 7 Harmonized Landsat Sentinel-2 tiles used for the single-year 2018-2019 analysis.

HLS Tile						
10SFJ	10SFH	10SGH	11SKB	11SKA	11SLA	11SLV
07/04/18	07/04/18	07/04/18	08/05/18	07/06/18	07/06/18	07/06/18
07/09/18	07/09/18	07/09/18	08/10/18	07/11/18	07/16/18	07/16/18
07/14/18	07/14/18	07/11/18	08/15/18	07/16/18	07/26/18	07/21/18
07/19/18	07/24/18	07/14/18	08/18/18	07/21/18	07/31/18	07/26/18
07/24/18	08/08/18	07/16/18	08/25/18	07/26/18	08/15/18	08/05/18
08/08/18	08/13/18	07/21/18	09/04/18	07/31/18	08/18/18	08/15/18
08/13/18	08/18/18	07/24/18	09/09/18	08/05/18	08/25/18	08/18/18
08/18/18	08/23/18	07/26/18	09/14/18	08/10/18	09/09/18	09/04/18
08/23/18	08/28/18	08/05/18	09/19/18	08/15/18	09/19/18	09/09/18
08/28/18	09/02/18	08/08/18	09/24/18	08/18/18	09/29/18	09/14/18
09/02/18	09/07/18	08/10/18	10/09/18	08/25/18	10/09/18	09/19/18
09/07/18	09/17/18	08/13/18	10/14/18	09/04/18	10/19/18	10/09/18
09/17/18	09/22/18	08/15/18	10/19/18	09/09/18	10/24/18	10/14/18
09/22/18	09/27/18	08/18/18	10/24/18	09/14/18	11/08/18	10/19/18
09/27/18	10/07/18	08/18/18	11/08/18	09/19/18	12/03/18	10/24/18
10/07/18	10/12/18	08/23/18	11/18/18	10/09/18	12/13/18	11/03/18
10/12/18	10/17/18	08/25/18	12/13/18	10/19/18	01/02/19	11/08/18
10/17/18	10/22/18	08/28/18	01/02/19	11/08/18	01/27/19	12/03/18
11/01/18	12/06/18	09/02/18	01/27/19	11/18/18	02/11/19	12/13/18
11/06/18	12/31/18	09/04/18	02/11/19	12/03/18	04/07/19	01/02/19
12/06/18	01/25/19	09/07/18	03/18/19	12/13/18	07/01/19	03/18/19
12/26/18	02/19/19	09/09/18	04/22/19	01/02/19		04/07/19
12/31/18	03/11/19	09/17/18	05/02/19	02/06/19		06/16/19
01/25/19	03/16/19	09/19/18	06/16/19	02/11/19		06/26/19
02/19/19	03/31/19	09/22/18		05/02/19		07/01/19
03/11/19	05/05/19	09/24/18		06/26/19		
03/16/19	06/04/19	09/27/18		07/01/19		
03/31/19		10/07/18				
06/04/19		10/09/18				
06/24/19		10/12/18				
		10/14/18				
		10/17/18				
		10/19/18				
		11/06/18				
		11/08/18				
		11/16/18				
		11/18/18				
		12/03/18				
		12/13/18				
		12/28/18				

12/31/18
01/02/19
01/25/19
01/27/19
02/11/19
02/19/19
02/21/19
03/11/19
03/13/19
03/16/19
03/18/19
03/31/19
04/12/19
04/27/19
05/02/19
06/04/19
06/06/19
06/11/19
06/26/19

Table S2. Image dates from the August image stack used for the multi-year analysis.

Sensor	Year	Month	Day
Landsat 5 TM	2000	8	20
Landsat 5 TM	2001	8	23
Landsat 5 TM	2003	8	13
Landsat 5 TM	2004	8	31
Landsat 5 TM	2006	8	21
Landsat 5 TM	2007	8	24
Landsat 5 TM	2008	8	10
Landsat 5 TM	2009	8	29
Landsat 5 TM	2010	8	16
Landsat 8 OLI	2013	8	8
Landsat 8 OLI	2014	8	27
Landsat 8 OLI	2015	8	14
Landsat 8 OLI	2018	8	6
Landsat 8 OLI	2019	8	9

Table S3. Single-year confusion matrix using fraction thresholds of 0.9.

		Validation (meter-resolution Google Earth imagery)			
		Annual Grass	Evergreen	Deciduous + Shadow	Unvegetated
Prediction (10 m Sentinel-2)	Annual Grass	29	0	5	0
	Evergreen	3	30	1	0
	Deciduous + Shadow	6	2	26	0
	Unvegetated	0	0	0	34

Table S4. Multi-year confusion matrix using fraction thresholds of 0.9.

		Validation (meter-resolution Google Earth imagery)		
		High → High	High → low	Low → high
Prediction (30 m Landsat)	Persistent	29	3	2
	Decrease	3	31	0
	Increase	3	0	31

Figure01
Click here to download high resolution image

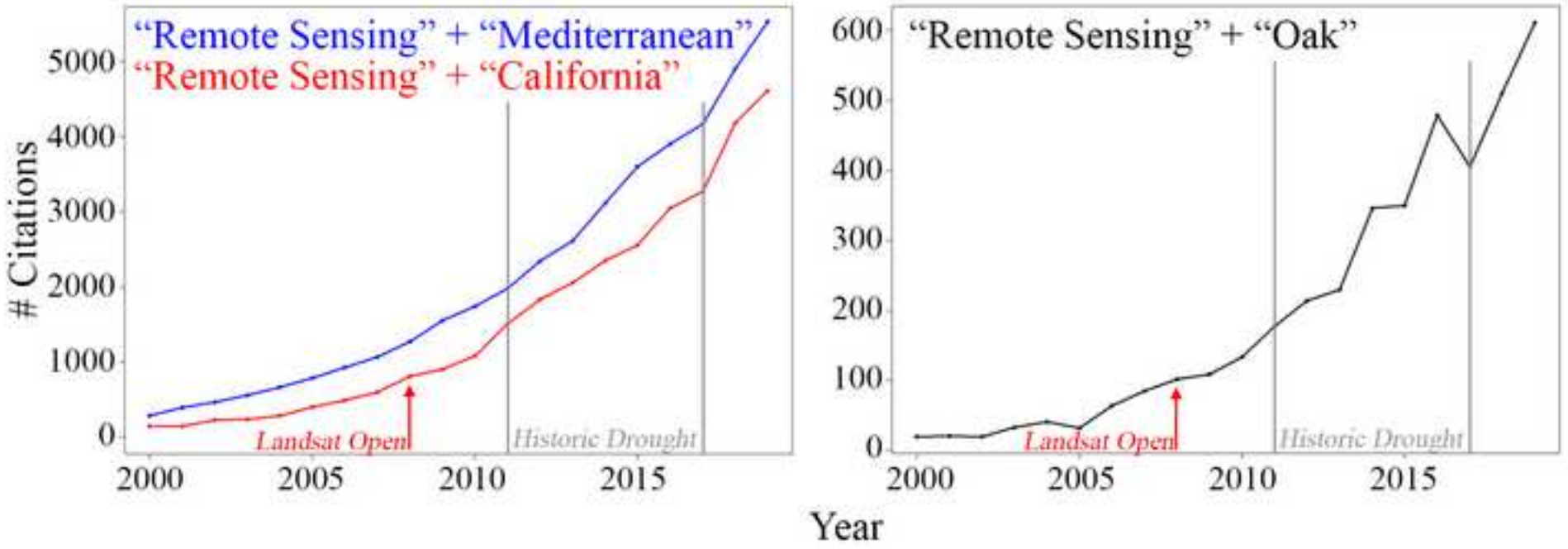

Figure 1. Citation history. Scientific interest in the remote sensing of Mediterranean landscapes (blue), remote sensing of California (red) and remote sensing of oaks (black), has shown a marked increase in recent years, as measured by number of citations in the Web of Science database associated with these keywords. Growth accelerated considerably following the 2008 opening of the Landsat archive (red arrows) and the 2011-2017 California drought (gray bars).

Figure02
Click here to download high resolution image

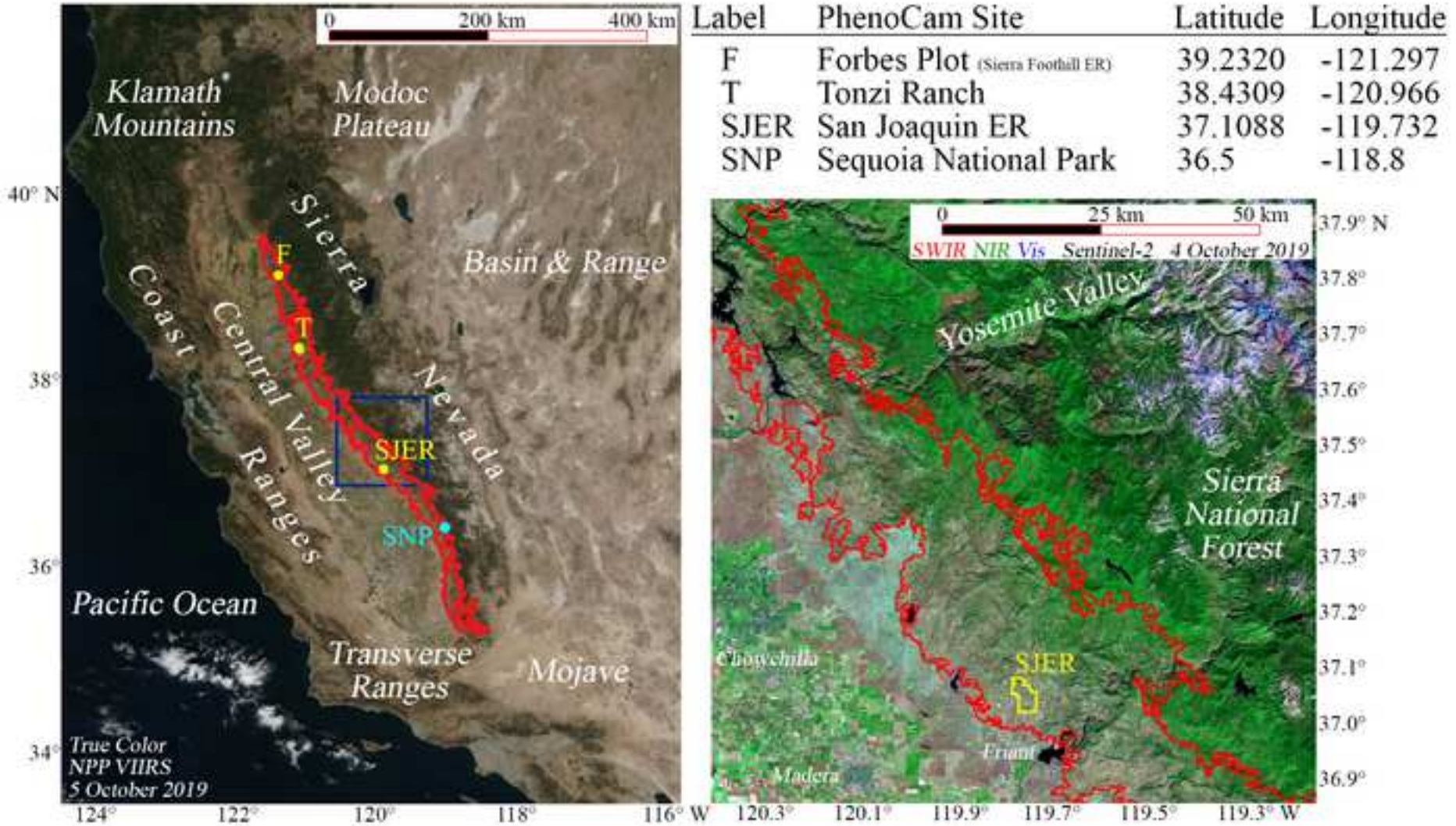

Label	PhenoCam Site	Latitude	Longitude
F	Forbes Plot (Sierra Foothill ER)	39.2320	-121.297
T	Tonzi Ranch	38.4309	-120.966
SJER	San Joaquin ER	37.1088	-119.732
SNP	Sequoia National Park	36.5	-118.8

Figure 2. Index map. Red outline shows approximate extent of Blue Oak (*Quercus douglasii*) in woodlands, savannas, and grasslands of the Sierra Nevada foothills. Yellow dots indicate PhenoCam locations used in Figures 4 and 5. Dark blue box and right panel show extent of the Sentinel-2 tile (11SKB) containing the San Joaquin Experimental Range (SJER, yellow vector), used for the single-year mapping example in Figures 6, 8a, 9 and 10. Cyan dot shows approximate location of foothill ecosystems within Sequoia National Park (SNP), site of multi-year analysis and validation example in Figures 7 and 8b.

Figure03
Click here to download high resolution image

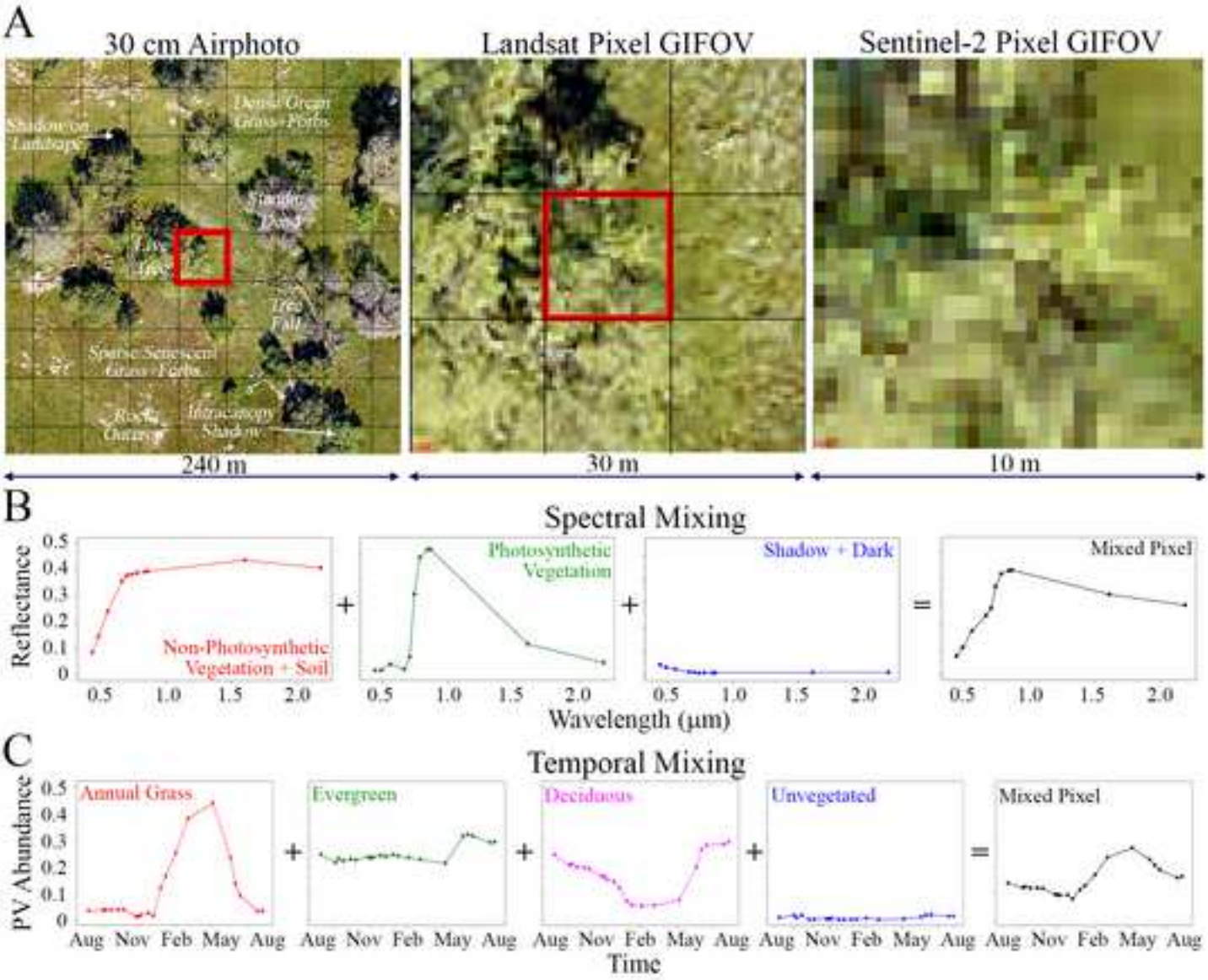

Figure 3. Subpixel mixing. A. Oak woodlands and savannas are spatially undersampled by decameter resolution sensors like Landsat and Sentinel-2. Example shown for the San Joaquin Experimental Range (SJER). When observed by low altitude airphotos (left), the landscape can be profitably segmented into discrete objects such as individual standing and fallen trees, rock outcrops, exposed soil, and grass/forb patches with varying composition. Shadowing is also evident both within plant canopies and from tall plants onto the adjacent understory. At the scale of 30 m Landsat/HLS and 10 m Sentinel-2 VNIR image time series, however, most pixels are comprised of varying mixtures of biotic and abiotic materials. B. Spectral mixture modeling estimates area abundance of spectrally distinct endmembers within each mixed pixel. C. Temporal mixture modeling simply extends this concept to the time domain, estimating subpixel area abundance of temporally distinct phenologies.

Figure04

Click here to download high resolution image

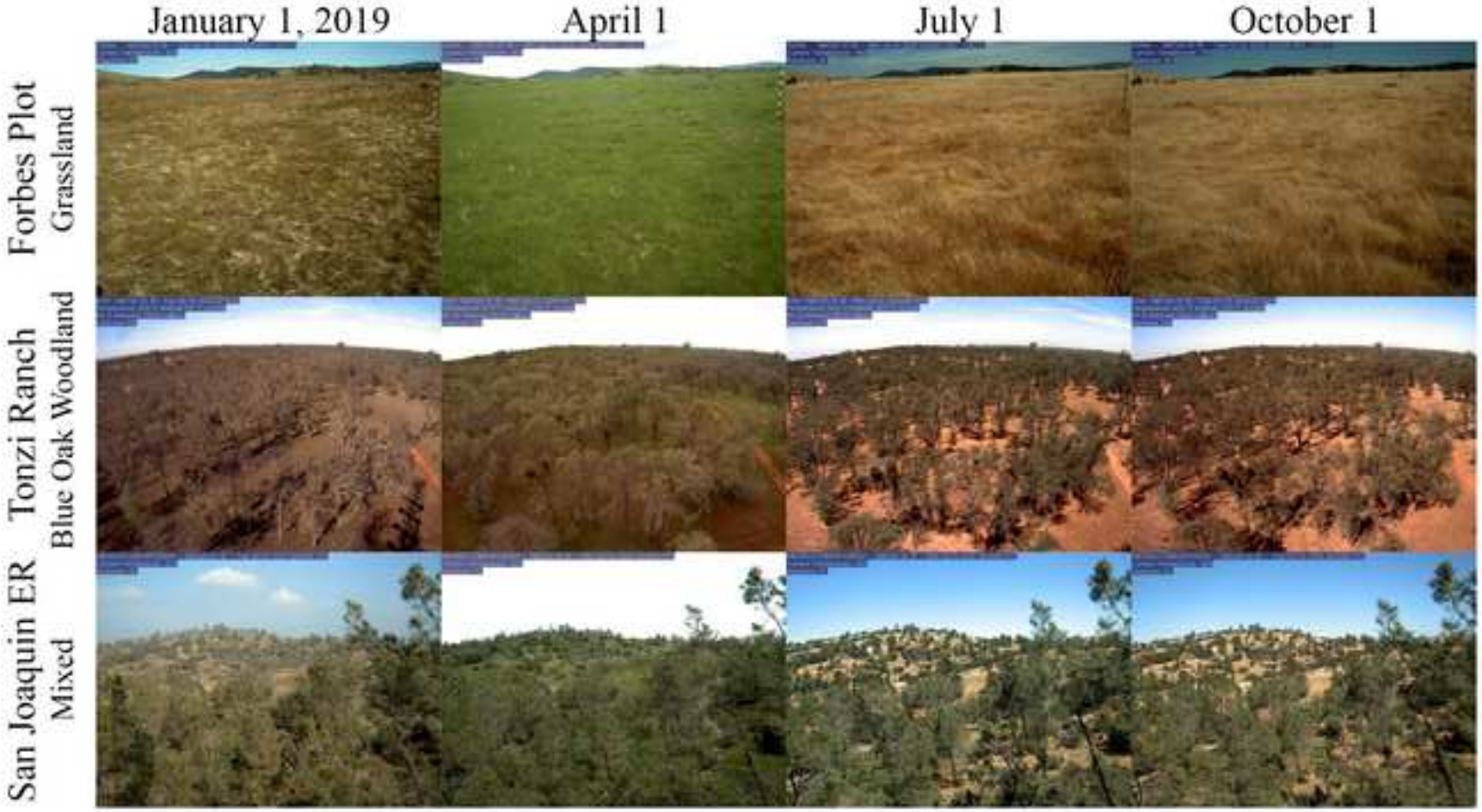

Figure 4. PhenoCam field photos. Oak density in Sierra foothill landscapes grades continuously from open, nearly treeless grasslands to closed woodlands. The PhenoCam network captures sites which span much of this range. Phenology of open grasslands (Forbes Plot at Sierra Foothill Experimental Range) is visibly different from that of oak-dominated woodlands (Tonzi Ranch). Evergreen conifers, visible in the mixed landscape of the San Joaquin Experimental Range, have yet different phenology. Typical annual cycles for each location are shown using mid-day images for each location. In areas dominated by annual grasses and deciduous oaks, maximum leaf cover (and primary production) occurs in the spring, when temperatures warm and the root zone water content is greatest. Non-native grasses senesce rapidly in late spring, but deciduous oaks (as well as some grasses, forbs, and shrubs) generally remain green through fall.

Figure05
Click here to download high resolution image

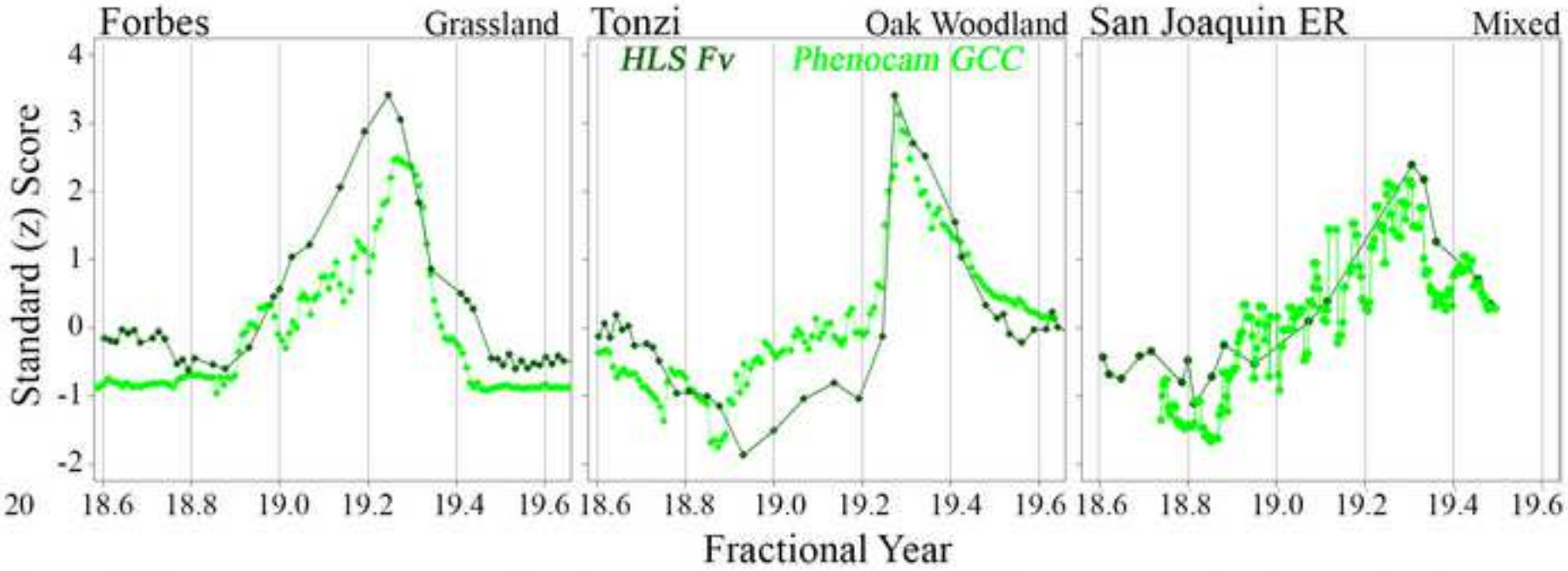

Figure 5. Phenocam versus satellite time series. The 2018-2019 water year is shown for the Forbes plot grassland (left), Tonzi Ranch blue oak woodland (center) and San Joaquin Experimental Range (right). 3-day average Green Chromatic Coordinate (GCC; lighter curve) from standard PhenoCam regions of interest is plotted with Harmonized Landsat-Sentinel (HLS) estimates of illuminated fraction of photosynthetic vegetation (Fv) from the pixels nearest the viewshed of each PhenoCam. For comparison, time series are normalized by transformation into Standard (z) Scores [i.e. $(x-\mu)/\sigma$]. Grasses show a gradual greenup throughout the winter, followed by abrupt senescence in late spring with diminishing water availability. Blue oak woodlands show loss of leaves in late fall/early winter and remain unvegetated until leaf on in spring. Evergreen/deciduous/annual landscape at SJER has a mixed phenology signal. The level of PhenoCam/HLS agreement is encouraging given differences in spatial coverage, sensing modalities and view angle. Corrlations are in the 0.8 to 0.9 range. Differences are likely due to a combination of BRDF effects and nonlinearities between the GCC and Fv metrics. The spectral mixture model also produces simultaneous estimates of two other land cover fractions (Substrate and Dark). Correlation between the Substrate fraction and PhenoCam Red Chromatic Coordinate (RCC) time series (not shown, 0.75 to 0.9) is also encouraging.

Figure06

Click here to download high resolution image

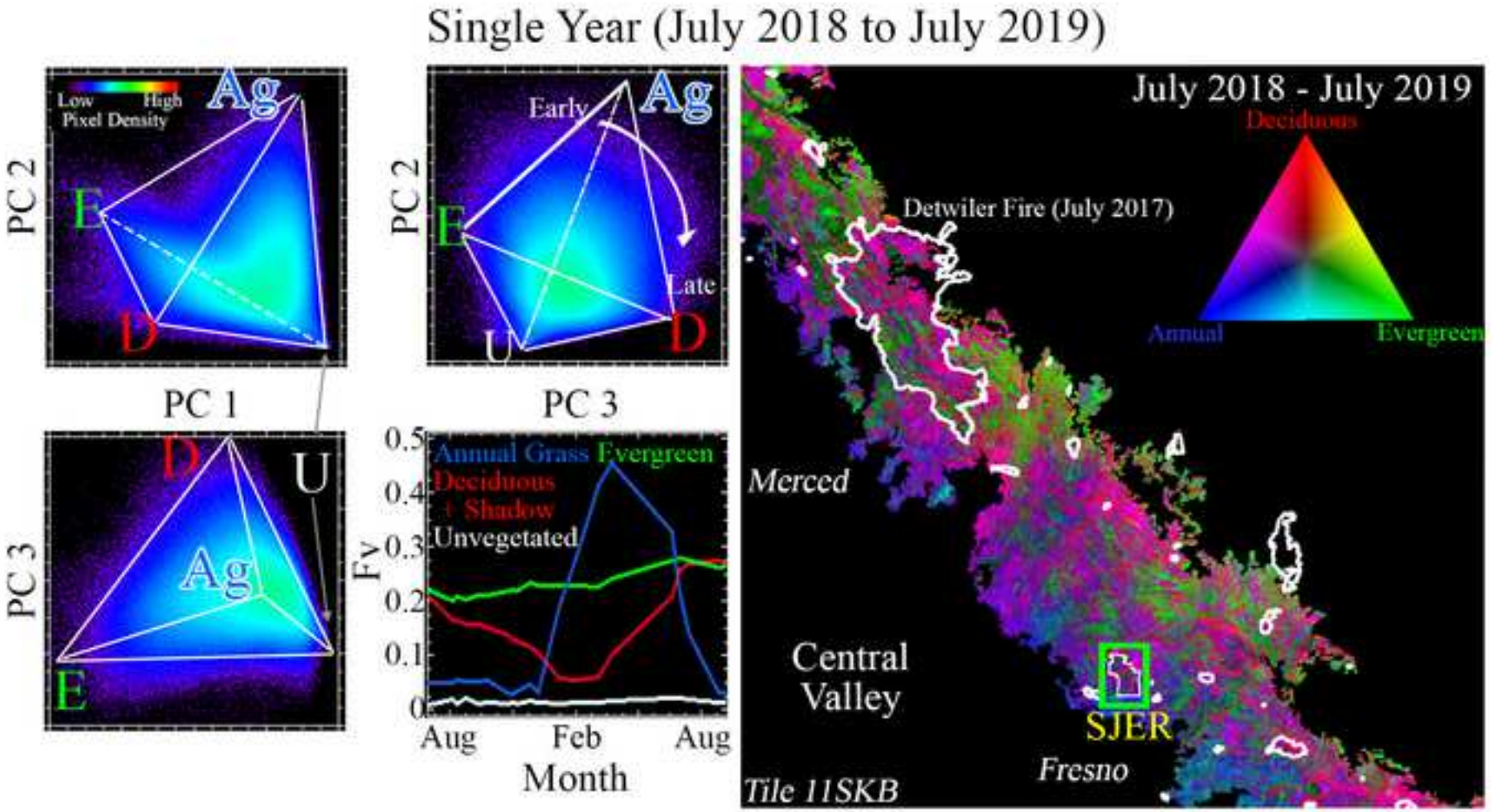

Figure 6. Single year example. The temporal feature space (TFS; left) and associated temporal mixture model (TMM; right) map are illustrated using a single year time series of vegetation abundance in tile 11SKB. The first three dimensions of the single year TFS clearly allow for discrimination between annual grasses (Ag), deciduous perennials + seasonal shadow (D), evergreen perennials (E), and unvegetated areas (U). Temporal endmembers (tEMs) representing each phenology are selected from the corners of the TFS and plotted in the lower right quadrant. These tEMs are then used to unmix the vegetation time series, generating a phenology map. The area surrounding San Joaquin Experimental Range (J; green box) is used for LiDAR comparison in Figure 8a. Fire perimeters (2015 onward) shown by white vectors.

Figure07
Click here to download high resolution image

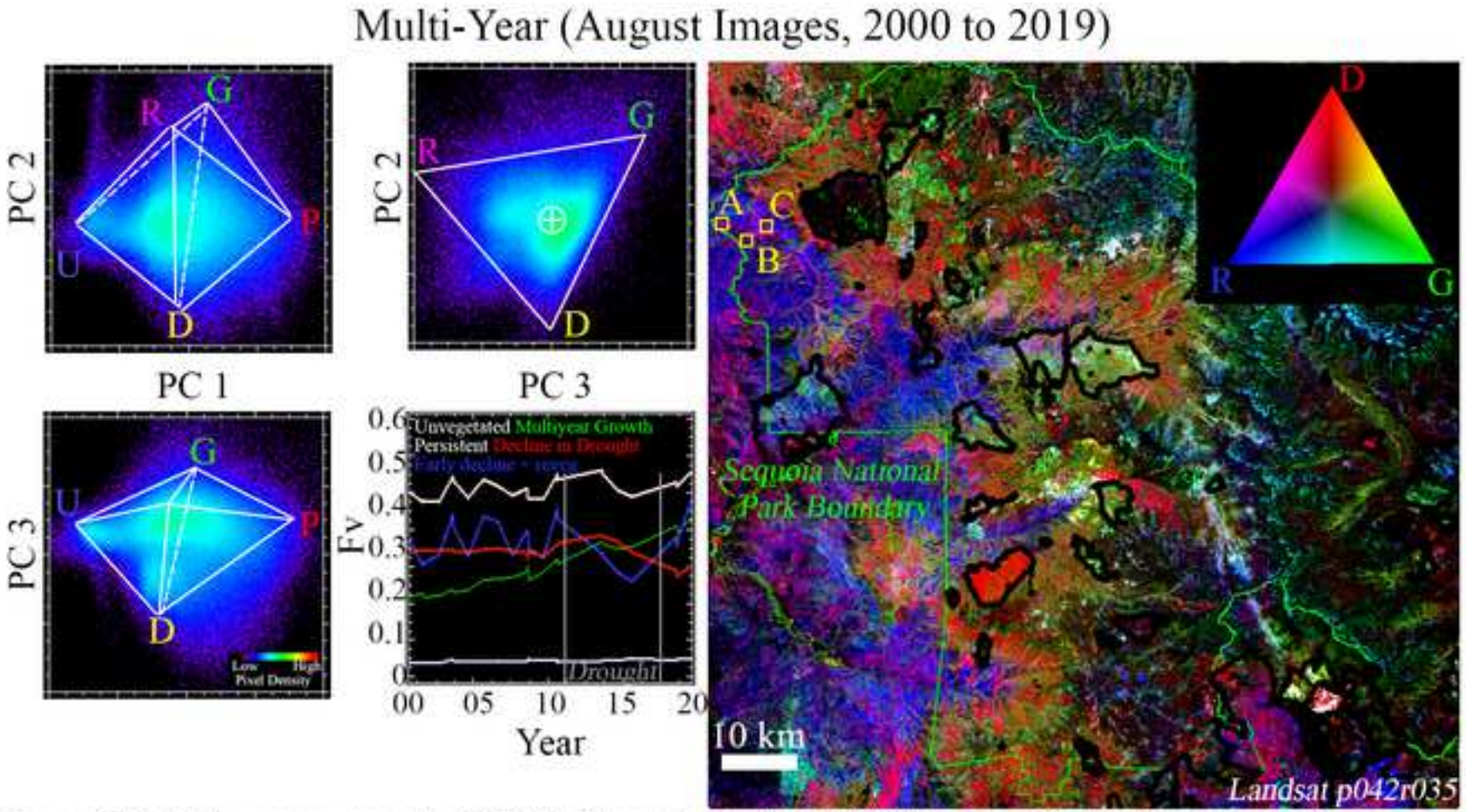

Figure 7. Multi-year example. TFS (left) and associated TMM map (right) show a multi-year change analog to the single-year phenology example from Figure 6. Model is based on a 20-year Landsat 5 and 8 time series of August vegetation abundance for Sequoia National Park and environs. Locations of example validation sites (A, B & C) shown in Figure 8b are indicated with yellow boxes. The low-order TFS forms a mixing space approximating a trigonal dihedral geometry, outlined by white lines. Temporal endmembers correspond to unvegetated (U; white), persistent (P; white), multiyear growth (G; green), decline during 2011-2017 drought (D; red), and decline in early years of drought followed by regrowth (R; blue). Beginning and ending of drought indicated by vertical gray lines. TMM shows spatial patterns corresponding to the R, D, and G tEMs. Park boundary shown with green vector and fire boundaries (1990-present) shown with black vectors.

Figure08a
Click here to download high resolution image

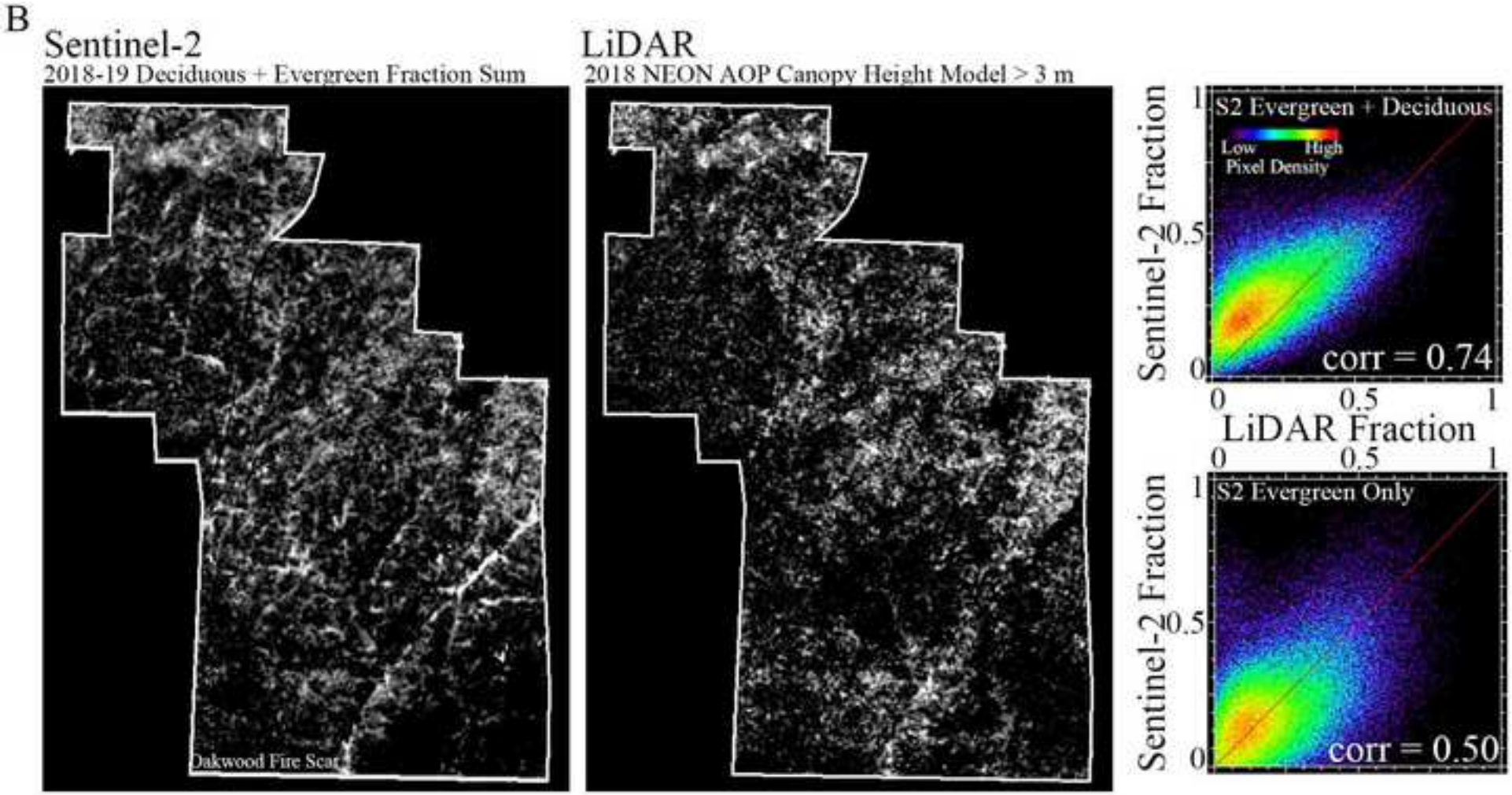

Figure 8a. Comparison of tree cover estimate to SJER LiDAR. Sentinel-2 single year evergreen + deciduous fraction sum correlates with 2018 NEON AOP LiDAR canopy height model >3 m at a level of 0.74. Sentinel-2 fractions slightly overestimate tree abundance at low fractions and underestimate tree abundance at high fractions. Correlation is substantially weaker for Sentinel-2 evergreen or deciduous fraction alone, as expected given mixed tree phenology.

Figure08b
Click here to download high resolution image

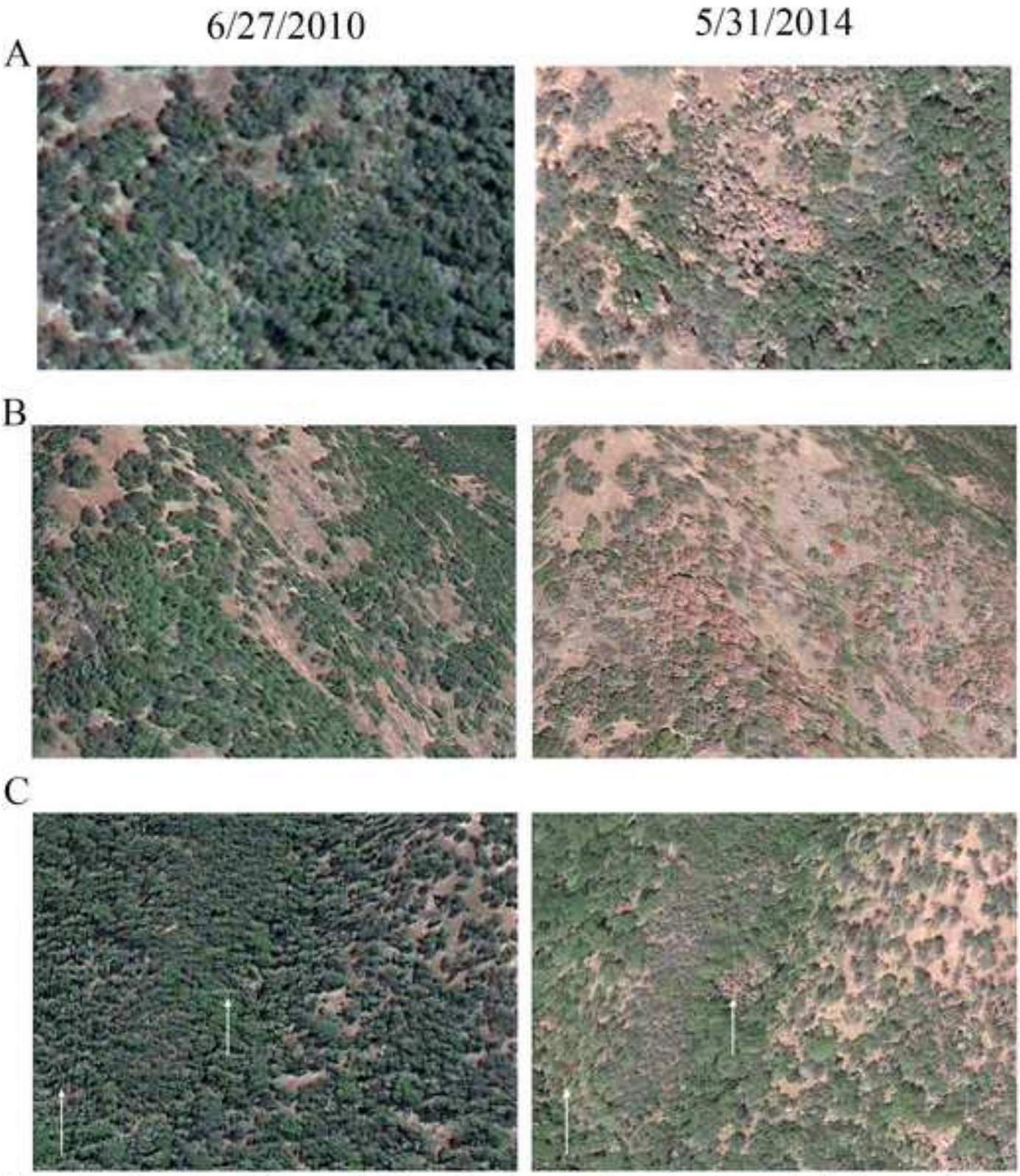

Figure 8b. Example multi-year validation. Visual comparison of meter-resolution imagery for locations indicated as decreasing through the drought. Image availability is limited, requiring the use of early summer (late May and late June) images. Despite this limitation, clear evidence of browning/defoliation is observed in 31 of the 34 areas indicated by the TMM as > 0.9 fraction of the Decrease temporal endmember. These results agree with the field measurements of (Das et al., 2020) and provide additional context in the form of spatial and temporal constraints on canopy loss.

Figure09

Click here to download high resolution image

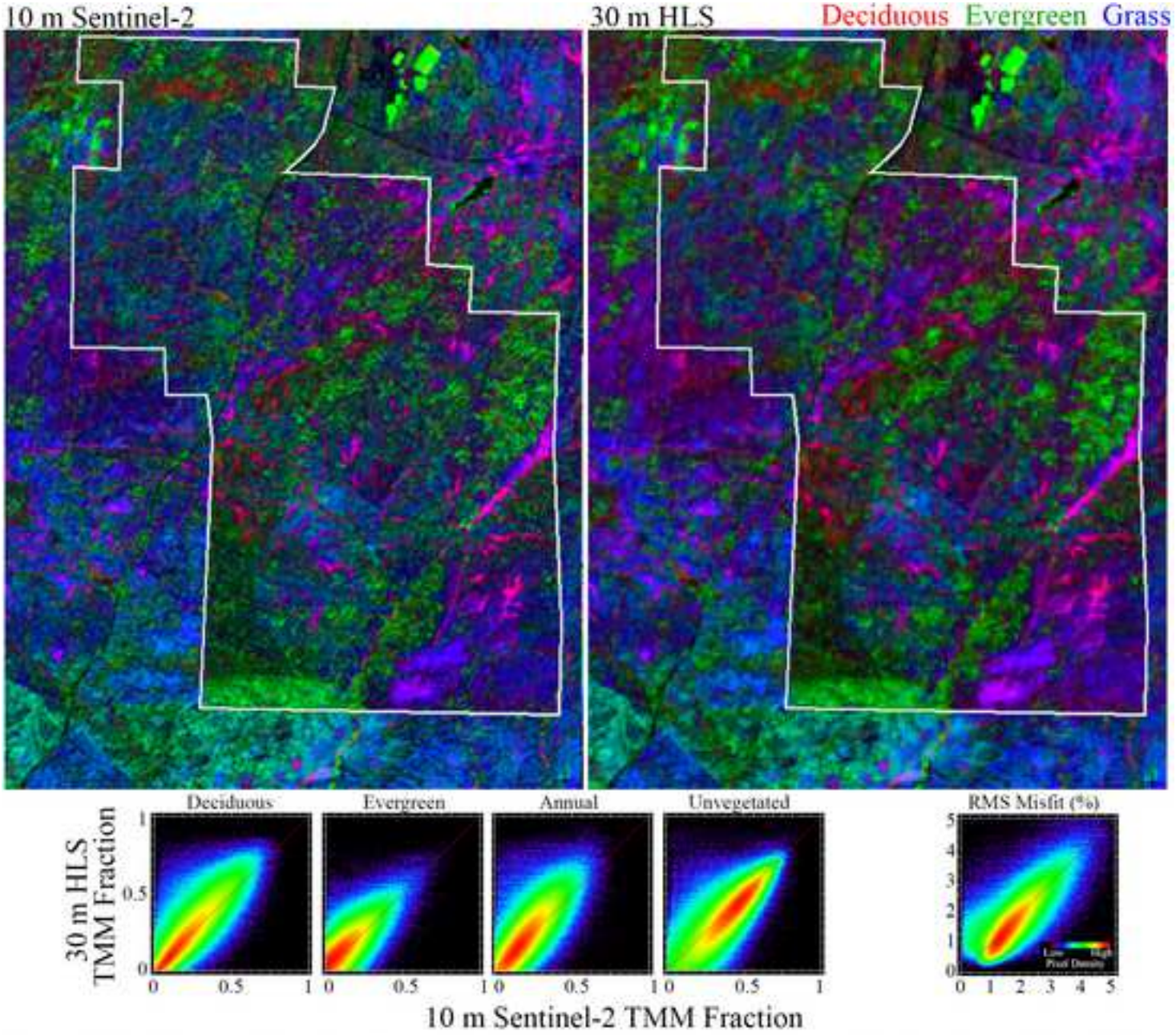

Figure 9. 10 to 30 m spatial scaling. Temporal mixture model fractions are compared for 10 m Sentinel-2 and 30 m Harmonized Landsat-Sentinel (HLS). Fractions generally scale linearly with correlations between 0.78 and 0.95. Minor bias between datasets is easily correctable with a linear transformation. This suggests that the temporal mixture model approach may be profitably applied for retrospective analysis at Landsat 4-8 spatial resolution.

Figure10

Click here to download high resolution image

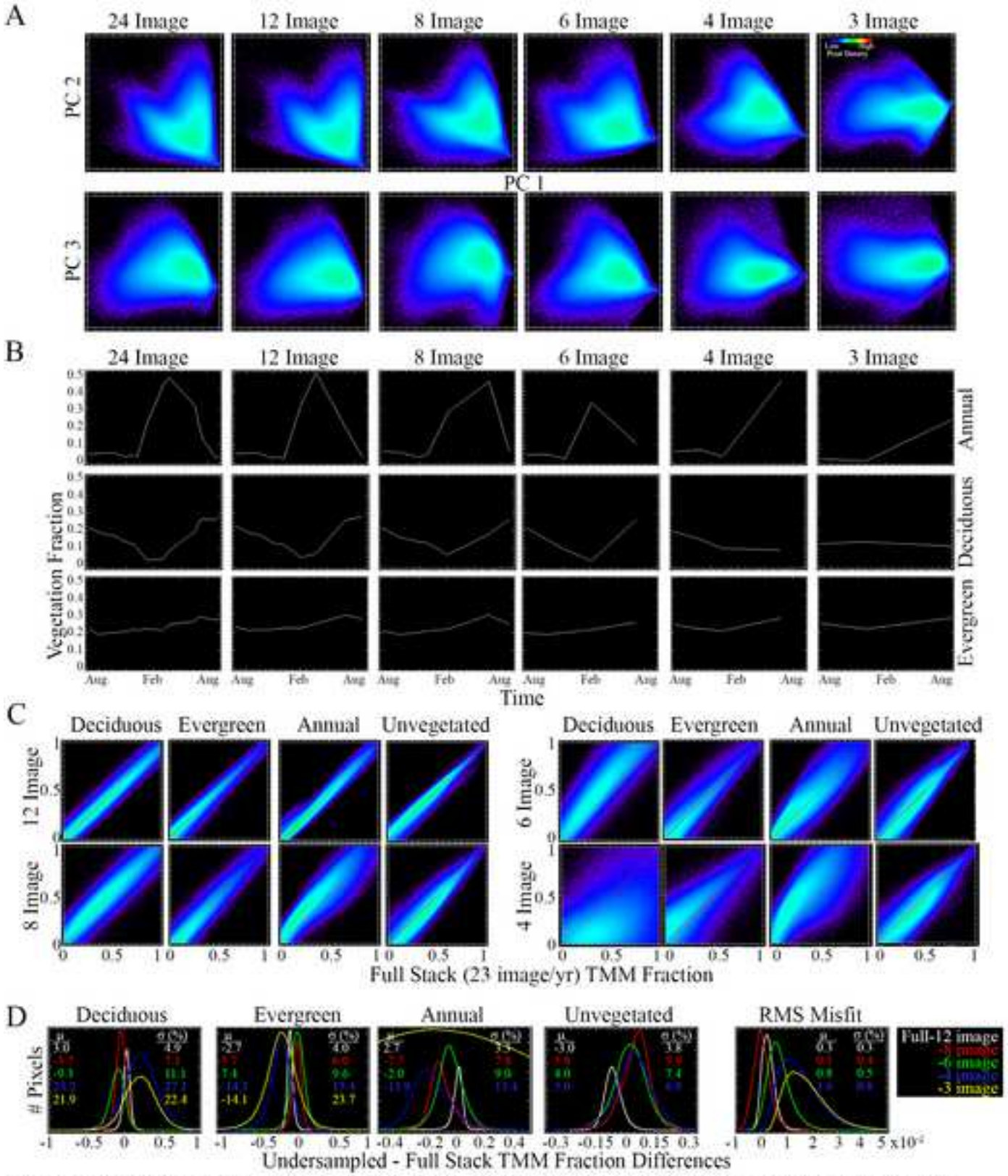

Figure 10. Temporal aliasing. Effect of degradation of temporal sampling on the single-year temporal feature space (A), temporal endmembers (B), and resulting temporal mixture model fractions (C and D) for the example HLS tile. PC 1 vs 3 topologic relations are generally retained with as few as 6 images. Fraction agreement remains linear down to the 6-image stack. Mean fraction differences are <10% for each fraction even when the temporal signal is degraded from 24 to 6 images per year. Degradation down to 4- and 3- images per year results in instability in the 4-EM inversion.

Figure11
Click here to download high resolution image

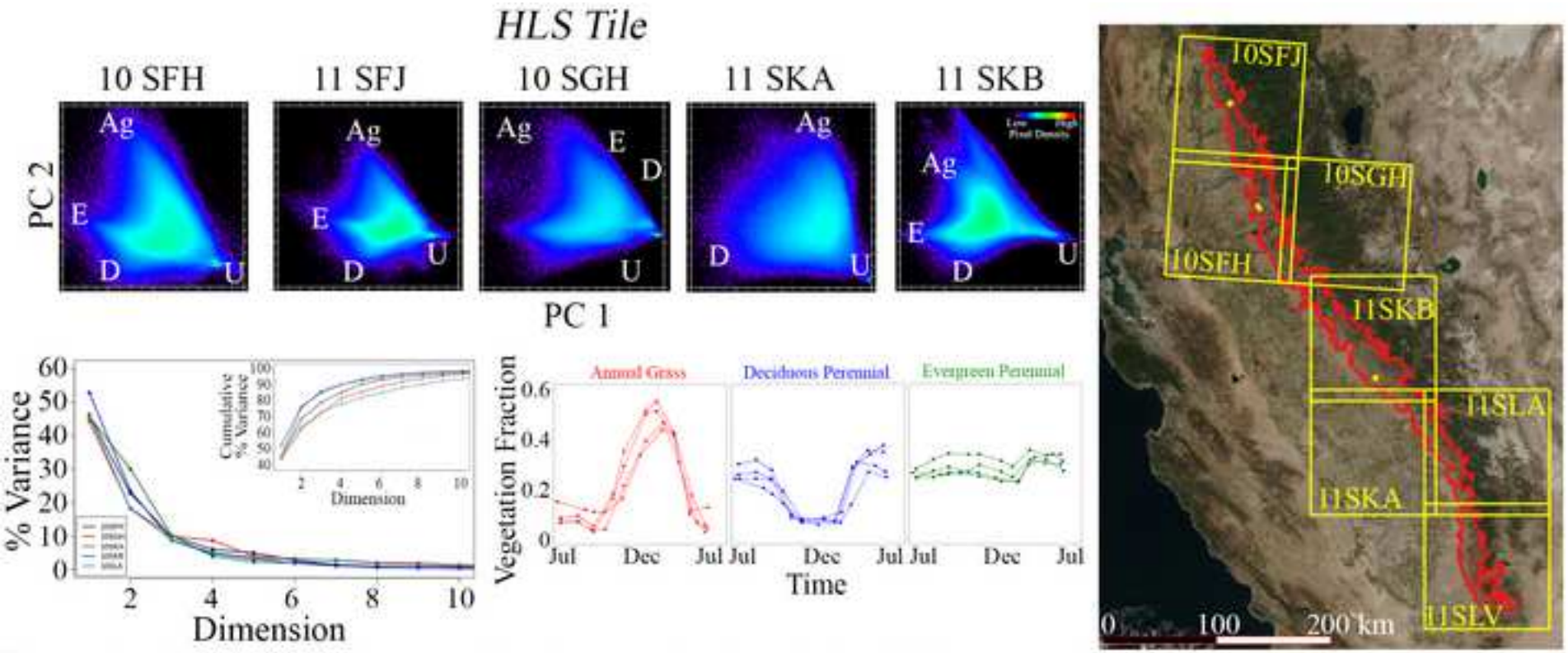

Figure 11. Cross-tile consistency. Despite spanning hundreds of kilometers, the low-order topology of the foothill oak woodland temporal feature space remains remarkably consistent across HLS tiles. Endmembers located on the PC 1 vs 2 projection represent corresponding phenological signals (evergreen, E; deciduous perennial; D, annual grass, Ag; and unvegetated, U) in each case. The sole exception is tile 11SKA, which does not show an E tEM because its spatial domain within the oak woodland mask does not include sufficient coverage of high elevations. Despite the consistency of the low-order temporal feature space, variation exists in higher dimensions, as revealed by the partition of variance (lower left). For instance, the first 2 dimensions to contain 62-75% of the overall variance in the dataset. The cumulative distribution of variance (inset) also shows this point. In some tiles (e.g. 10SFH), 90% of data variance is contained in the first 4 dimensions; other tiles (e.g. 10SLA) require as many as 10 dimensions to capture 90% of data variance. Tile 11SLA and 11SLV are not shown for brevity.

***Declaration of Interest Statement**

Declaration of interests

☒ The authors declare that they have no known competing financial interests or personal relationships that could have appeared to influence the work reported in this paper.

☐The authors declare the following financial interests/personal relationships which may be considered as potential competing interests: